Interaction between eye movements and adhesion of extraocular muscles

Hongmei Guo[a,b,1*], Yunfei Lan[a,1], Zhipeng Gao[a], Chenxi Zhang[a], Liping Zhang[a], Xiaona Li[a], Jianying Lin[a], Ahmed Elsheikh[c], Weiyi Chen[a*]

[a] College of Biomedical Engineering, Taiyuan University of Technology, Taiyuan 030024, China;
[b] Third Hospital of Shanxi Medical University (Shanxi Bethune Hospital, Shanxi Academy of Medical Sciences, Tongji Shanxi Hospital), Taiyuan 030032, China.
[c] School of Engineering, University of Liverpool, Liverpool, United Kingdom
[*] Correspondence: guohongmei@tyut.edu.cn; chenweiyi@tyut.edu.cn
[1] These authors contributed equally to this work.

Abstract

The adhesion between the extraocular muscles and the sclera affects eye movement. The contact and pull-off tests and finite element simulations were used to study the extraocular muscle-sclera adhesion and its variation with eye movement in this research. The effect of the adhesion on the eye movements was also determined using equilibrium equations of eye motion. The contact and pull-off tests were performed using quasi-static and non-quasi-static unloading velocities. Finite element models were developed to simulate these tests in cases with high unloading velocity which could not be achieved experimentally. These velocities range from the eye's fixation to saccade movement. The tests confirmed that the pull-off force is related to the unloading velocity. As the unloading velocity increases, the pull-off force increases, with an insignificant increase at the high ocular saccade velocities. The adhesion moment between the extraocular muscles and the sclera exhibited the same trend, increasing with higher eye movement velocities and higher separation angles between the two interfaces. The adhesion moment ratio to the total moment was calculated by the traditional model and the active pulley model of eye movements to assess the effect of adhesion behavior on eye movements. At the high ocular saccade velocities (about 461 deg/s), the adhesion moment was found to be 0.53% and 0.50% of the total moment based on the traditional and active pulley models, respectively. The results suggest that the adhesion behavior between the extraocular muscles and the sclera has a negligible effect on eye movements. At the same time, this adhesion behavior can be ignored in eye modeling, which simplifies the model reasonably well.

Keywords: Adhesion behavior, Extraocular muscle, Eye Movement, Viscoelasticity, Finite element.

1. Introduction

During the eye movement, the extraocular muscle (EOM) regulates the rotation of the eyeball, leading to an inevitable contact and separation process between the surface of the sclera and the EOM, which results in adhesive interactions. Previous studies have investigated the material properties of EOM along the length direction (including strength, tangent modulus, and toughness), but have neglected the properties in the thickness direction of the EOMs and the adhesion properties between the sclera and the EOMs [1-5].

The adhesion behavior of biological tissues is commonly assessed using contact and pull-off tests, where a rigid indenter is brought into contact pressed into the test material, and subsequently separated [6-8]. Dai et al. investigated the adhesion behavior of facial skin using contact and pull-off tests, revealing variations in adhesion behavior under different moisture conditions [9]. Similarly, Zhu et al. conducted contact and pull-off tests on silicone hydrogel contact lenses while on the cornea, demonstrating that different lens materials affected the lens-cornea adhesion differently [10]. In a more recent study, contact and pull-off tests were employed to determine the adhesion behavior between the retina and the vitreous, which was identified as a significant factor contributing to rhegmatogenous retinal detachment [11].

The theoretical foundation of contact and pull-off tests can be traced back to the early research conducted by Kendall and colleagues, specifically the Johnson-Kendall-Roberts (JKR) model [12-14]. The JKR model primarily describes the contact mechanics between two elastic solids or an elastic solid and a substrate of another material, where under the influence of Hertzian contact pressure, adhesive forces are generated and result in a necking-like deformation in the contact region, thereby increasing the contact area. According to the JKR model, contact stresses gradually approach infinity at the contact edge, and the resulting pull-off force during separation is given by $P_{pull-off} = -1.5\pi R\Delta\gamma$, where R denotes the radius of the indenter while $\Delta\gamma$ represents the work of adhesion. The elastic behavior of adhesive contacts can also be characterized by the Tabor parameter μ [15], which can be expressed as

$$\mu = \left[\frac{R\Delta\gamma^2}{E^{*2} z_0^3} \right]^{1/3}$$

where $E^* = \left[\left(1-\nu_1^2\right)/E_1 + \left(1-\nu_2^2\right)/E_2 \right]^{-1}$ is the equivalent elastic modulus (E_1, ν_1 and E_2, ν_2 denote the elastic modulus and Poisson’s ratio of the two contacting elastic spheres, respectively) and z_0 represents the equilibrium distance. As reported in earlier research, the JKR model is valid for cases in which $\mu > 5$, a condition that applies to this study [16].

Soft materials can be broadly categorized as either elastic or viscoelastic. The JKR theory is primarily applicable to elastic soft materials. However, the analysis becomes more complex when dealing with viscoelastic materials due to the consideration of velocity dependence.

In cases of viscoelastic materials, even when unloading velocity approaches zero, the JKR theory can still be utilized to evaluate their behavior. This theory gains importance when studying the adhesion between two viscoelastic materials during separation. Under specific conditions, an increase in velocity-induced adhesion is observed due to the velocity-dependent properties inherent to viscoelasticity, which are absent under quasi-static conditions [17-19]. This phenomenon has been well-documented across various viscoelastic materials, highlighting the influence of strain rate [20, 21].

Notably, Muller's work highlights that when viscoelastic spheres come into contact with a plane, pull-off forces can significantly exceed the thermodynamic predictions from the JKR theory, and this discrepancy exists even at minimal separation velocities [22]. Steady fixation velocities are less than 2 deg/s (26 mm/min), smooth pursuit tracks moving targets at velocities below 70 deg/s (911 mm/min), and the peak saccade velocity is up to 600 deg/s (7806 mm/min) [23, 24]. Since the velocities of some eye movements may be outside the quasi-static velocity range (higher than 30 mm/min), these movements may surpass the applicability limits of the traditional JKR theory [24-26]. Therefore, it is necessary to adopt the JKR-like viscoelastic model in this study to accommodate the velocity dependence due to the tissue's viscoelastic behavior.

In this context, Afferrante and Violano conducted a significant study using a JKR-like test between an optical spherical glass lens and a viscoelastic rubber substrate [27]. They developed an analytical solution based on the JKR theory, offering insights into the detachment of a rigid sphere from a viscoelastic substrate [28]. This solution provides a nuanced understanding of viscoelastic adhesion behavior by presenting applied load and contact penetration as functions of the contact radius, thus enabling a more accurate representation of velocity dependent viscoelastic detachment.

In addition to theoretical analysis, the finite element method serves as a valuable tool for simulating interfacial adhesion. For instance, He conducted finite element simulations to investigate the detachment of a spherical indenter from an elastic film [29]. This study identified the key factors governing interfacial instability modes and proposed methods to hinder such instabilities. Jiang developed a finite element model to explore the contact between a polydimethylsiloxane (PDMS) stamp substrate and a spherical viscoelastic adhesive indenter [30]. The study showed that the rate dependence became more pronounced at higher unloading velocities. Afferrante and Violano investigated classical Hertzian contact adhesion using a finite element approach, incorporating adhesive interactions described by the Lennard-Jones potential and viscoelastic behavior described by a standard linear solid model [31, 32]. Their study revealed a significant velocity dependence of the adhesion force.

The effect of the adhesion behavior of the EOM to the sclera on eye movements can be assessed by modeling eye movements. In the study of eye movement models, the perception of eye movement was changed by the discovery of the pulley, a connective tissue of the EOM bonded to the orbital wall, the presence of which altered the path of force on the EOM. Currently, two common models are used in eye movement modeling: the traditional (non-pulley) model and the active pulley model. In the traditional model, the EOMs are constituted by several key points: the insertion point, the tangent point, and the origin point (the end where the EOM is attached to the bony orbit) [33]. Demer et al. proposed the active pulley hypothesis, which views the location of the pulley as a functional origin for eye movements, with the functional origin moving with the eye during eye movements [34]. Many reviews have described active pulley behavior and emphasized that pulleys are the functional origin of EOM [35-38]. In this study, the EOM behavior in the thickness direction was determined in compressive stress-relaxation tests. The study also quantified the adhesion behavior between the EOM and the sclera using experimental and finite element analysis methods. The effect of this adhesion on eye movement was then quantified by calculating the ratio between the adhesion moment, and the total moment using the traditional model and the active pulley model.

2. Materials & methods

2.1 Specimens preparation

A total of 180 porcine eyes, of animals aged between 6 and 8 months, were procured from a local slaughterhouse and promptly transported to the Laboratory of Soft Tissue Biomechanics, Taiyuan University of Technology, within 24 hours post-mortem. The eyes were placed in an ice pack during transport, preventing dehydration and tissue decay. At room temperature, the EOMs were dissected from each eye using scissors and forceps, and subsequently cut into strips with dimensions of (24.3 ± 3.4 mm) × (10.2 ± 2.2 mm) × (2.5 ± 0.5 mm). In making an EOM specimen, the fat was carefully removed and the membrane on the surface of the EOM was preserved. We chose the portion of the sclera posterior to the EOM insertion point for scleral specimen preparation, which was positioned between the anterior and equatorial portions of the sclera. The sclera was cut into a specimen twice the radius of the indenter with surgical scissors. The circular sclera specimens are shown in Fig. 1. The indenter was dipped in glue and bonded to the sclera, and the excess of the scleral specimen was cut off. Before conducting the contact and pull-off tests, the thickness at the center of the sclera specimens was measured three times using a laser displacement sensor (LK-H050, Keyence Corporation). The thickness of the sclera was recorded as 0.55 ± 0.23 mm.

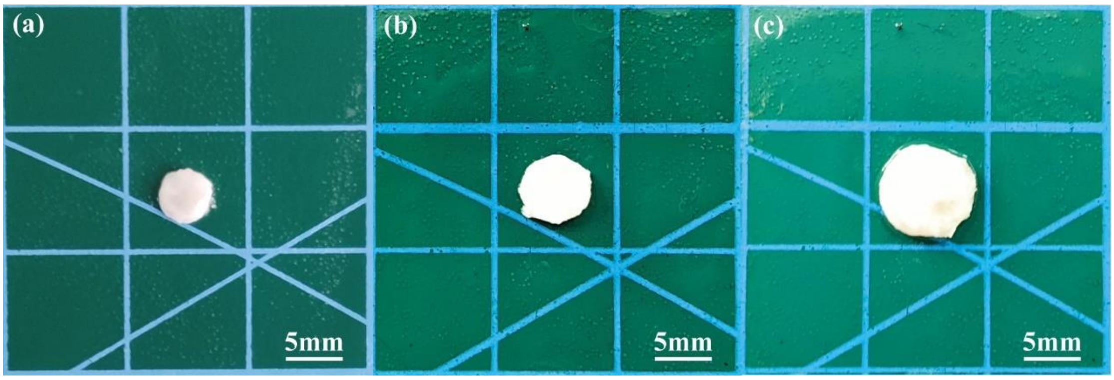

Fig. 1. The shape and size of the porcine sclera tissue specimens. Scale bars are labeled in the lower right corner of the figure. Scleral specimens bonded at indenter radii of **(a)** 1 mm, **(b)** 1.5 mm, and **(c)** 2 mm are shown.

2.2 Contact and pull-off tests

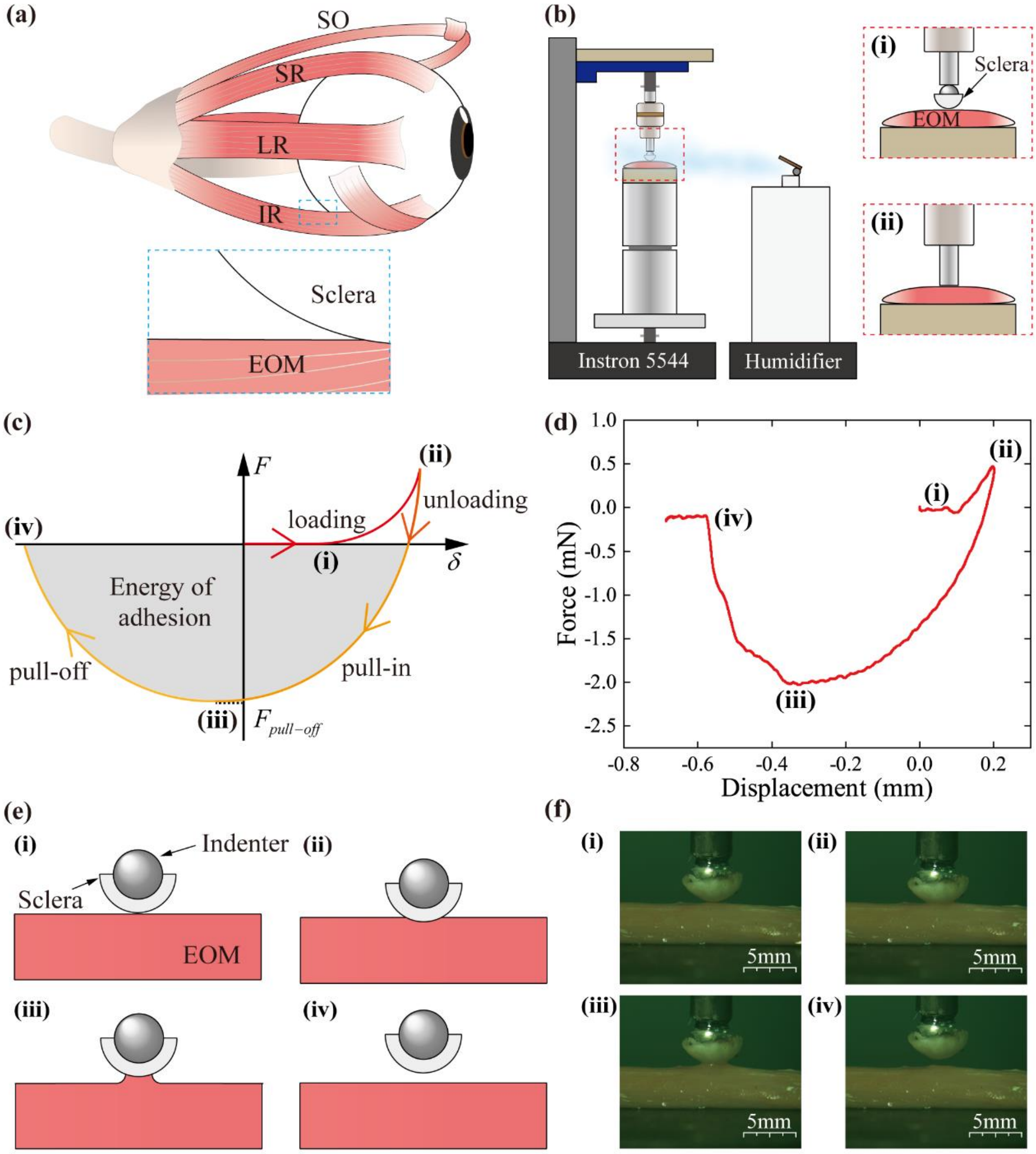

Fig. 2. The adhesion behavior between the sclera and the EOMs. **(a)** The EOMs responsible for controlling eye movements include the lateral rectus (LR), medial rectus (MR), superior rectus (SR), and inferior rectus (IR) muscles, as well as the superior oblique (SO) and inferior oblique (IO) muscles. The inset provides a visual representation of the adhesive interaction hypothesis between the sclera and EOMs during eye movements. **(b)** Schematic of Instron 5544 testing machine. The illustration is a partial enlargement of the specimen. **(i)** Contact between the scleral

tissue-wrapped indenter and the EOM in the contact and pull-off tests. **(ii)** Contact between the flat-ended indenter and the EOM in the compressive stress-relaxation tests. **(c)** A diagram outlines the contact and pull-off test procedure, including **(i)** the loading phase, **(ii)** maximum compression force, **(iii)** pull-off force, and **(iv)** separation. **(d)** The adhesion force-displacement diagram of a typical specimen, with an unloading velocity of 6 mm/min. **(e)** A schematic diagram illustrates the different phases of the contact and pull-off test. **(f)** Experimentally captured images depict the various phases of the contact and pull-off test. The scale bar is labeled in the lower right corner.

The EOMs responsible for controlling eye movements include the lateral rectus (LR), medial rectus (MR), superior rectus (SR), and inferior rectus (IR) muscles, as well as the superior oblique (SO) and inferior oblique (IO) muscles. Physiologically, the EOMs wrap around the sclera, with adhesive interaction between the two tissues due to their viscoelastic nature (Fig. 2.a). To investigate the adhesion behavior between the sclera and the EOMs at room temperature, contact and pull-off tests were conducted.

The contact and pull-off tests were performed using an Instron 5544 (Instron, Boston, USA) testing machine, equipped with a load cell with 5 N capacity and 0.001 N accuracy (Fig. 2.b). In preparation, the sclera specimens were glued onto spherical indenters with radii of 1 mm, 1.5 mm, and 2 mm. The test process then commenced as follows:

(i) The scleral tissue-wrapped indenter moved towards the EOM tissue at a velocity of 1 mm/min until contact was established.

(ii) The scleral tissue-wrapped indenter was pressed into the EOM to achieve a maximum indentation of 0.1 mm. The force corresponding to this displacement is referred to as the preload force. Subsequently, the scleral tissue-wrapped indenter was pulled away from the EOM with unloading velocities that included quasi-static velocities of 0.5, 1, 6, 18, and 30 mm/min; and non-quasi-static velocities of 42 and 300 mm/min. The number of EOM specimens used in the above experiment is shown in Table 1.

Table 1. Number of EOM specimens with different unloading velocities for contact and pull-off tests.

Indenter radius	**0.5 mm/min**	**1 mm/min**	**6 mm/min**	**18 mm/min**	**30 mm/min**	**42 mm/min**	**300 mm/min**
1 mm	31	28	30	29	27	31	27
1.5 mm	35	25	28	29	30	32	28
2 mm	26	30	26	27	29	28	29

(iii) As the scleral tissue-wrapped indenter detached from the EOM, peeling occurred at or near the maximum adhesive force (Pull-off force $F_{pull-off}$).

(iv) Finally, the scleral tissue-wrapped indenter completely separated from the EOM, and the force measured by the sensor returned to zero.

The entire experimental process was carefully observed and documented using a charge-coupled device (CCD) for image acquisition. Fig. 2.c shows a schematic diagram of the contact and pull-off tests including the four steps described above.

Data collection started when the gap between the sclera and the EOM was 0.1 mm, and the indenter was then displaced towards the EOM specimen for 0.2 mm leading to a maximum indentation of 0.1 mm, before reversing the loading direction. Fig. 2.d shows the adhesion force-displacement diagram of a typical specimen, with an unloading velocity of 6 mm/min.

Furthermore, to evaluate the effect of air exposure duration on the EOM-sclera adhesion behavior, EOM strips were acquired and divided into two groups – with 30 specimens each – one with 15 min exposure, and one with 30 min exposure – both groups were subjected to an unloading velocity of 0.5 mm/min. Exposure time refers to the time from the dissection to the end of the test, corresponding to the entire procedure of strabismus surgery. The number of EOM specimens used in the above experiments is shown in Table 2.

Table 2. Number of EOM specimens with different exposure times for contact and pull-off tests.

Indenter radius	Exposure time 15min	Exposure time 30min
1 mm	31	25
1.5 mm	35	28
2 mm	26	23

In all tests, two parameters were of particular interest: First, the $F_{pull-off}$ at stage **(iii)**, which prevented the EOM-sclera separation; Second, the work of adhesion, $\Delta\gamma$, defined as the work required per unit area to separate the two tissues from initial contact to infinite separation. This parameter is crucial in characterizing the strength of adhesion between the two tissues. To determine $\Delta\gamma$, the adhesion energy, U, was obtained first by integrating the attraction region of the behavior curve (gray area in Fig. 2.c). Subsequently, U was divided by the contact area to determine $\Delta\gamma$. Fig. 2.e presents a schematic diagram illustrating this process, while Fig. 2.f shows images of the contact and pull-off test.

2.3 Compressive stress-relaxation test

In this study, uniaxial compressive stress-relaxation tests were conducted on porcine EOMs, where the EOMs were subjected to compressive loads along the thickness direction. The EOM specimen did not slide on the test bench during the test. A total of 14 EOM specimens were tested using an Instron 5544 tester. A flat-ended indenter with a diameter of 5 mm was used at 1 mm/min to compress the specimens with a compressive strain of 10%. The schematic diagram of a flat-ended indenter compressed into the EOM is shown in Fig. 2.b. After the ramp loading phase, the compression was held constant for 500 seconds to allow the specimens to stress-relaxation. Each specimen was tested only once. Considering the elevated levels of strain, such as that applied in our tests, can result in permanent tissue deformation, no preload was applied. Additionally, a humidifier was used throughout to make sure that the tissue did not dehydrate.

2.4 Theoretical Analysis

2.4.1 JKR-like viscoelastic model

In the seminal work by Johnson, Kendall, and Roberts, an analytical closed-form solution was developed to characterize adhesive contact between a rigid sphere and an elastic, soft half-space [12]. The JKR theory provides straightforward expressions that establish relationships between the applied load F, indentation displacement δ, and contact radius a. However, in the context of viscoelastic materials, an equivalent solution does not exist, necessitating the utilization of numerical or semi-analytical methods to address the problem [28].

When the approach and retraction phases are performed under quasi-static conditions, the viscoelastic substrate behaves as an elastic medium. For an elastic substrate, F and δ can be determined in terms of a by JKR theory

$$F = \frac{4}{3}\frac{E^* a^3}{R} - \sqrt{8\pi E^* a^3 \Delta\gamma} \tag{1}$$

$$\delta = \frac{a^2}{R} - \sqrt{\frac{2\pi a \Delta\gamma}{E^*}} \tag{2}$$

where E^* is the equivalent elastic modulus, $\Delta\gamma$ is the work of adhesion, which depends on the adhesion properties of the contact interface, and R is the radius of the indenter.

In the presence of a viscoelastic substrate, the process of detachment involves the occurrence of viscous dissipation. Gent and Schultz introduced the concept of an equivalent work of adhesion $\Delta\gamma_{eff}$ to account for this dissipation [39]. An empirical relationship known as the Gent-Schultz law is often used to describe crack propagation, which is similar to the separation process between the sclera and the EOM. The $\Delta\gamma_{eff}$ was found to be dependent on the velocity of loading and is typically expressed as a function of the contact line velocity $v_c = -da/dt$ [40, 41]. This dissipation function is characteristic of viscoelastic materials and is not influenced by the geometry of the contact. These observations can be explained by the following empirical equation.

$$\Delta\gamma_{eff} = \Delta\gamma\left[1 + \left(\frac{v_c}{v^*}\right)^n\right] \tag{3}$$

The crucial point to note is that the effective adhesion energy relies on the crack front velocity, denoted as the characteristic velocity v^* and the power-law exponent n, which can be determined through experimental measurements [19, 22, 39]. It is important to highlight that the exponent n is not a universal value but varies depending on the viscoelastic modulus [22, 42]. Generally, values for n typically range from 0.1 to 0.8 [43]. However, some arguments have been put forward suggesting that it is linked to the distribution of characteristic relaxation times within the viscoelastic material [44].

To accurately characterize the detachment behavior, it is necessary to determine the precise parameters of the contact line velocity v_c and the contact radius a. Considering that the pulling velocity is denoted as $V=-d\delta/dt$, the derivative $da/d\delta$ can be numerically calculated by solving a differential equation given by Muller [22], while Violano et al. estimated $da/d\delta$ from the JKR solution [45].

$$v_c = V\left(\frac{2a}{R}-\sqrt{\frac{\pi\Delta\gamma}{2aE^*}}\right)^{-1} \tag{4}$$

Due to the difficulty of experimental measurements, Eq. (4) was used to calculate the approximate value of v_c. The $\Delta\gamma_{eff}$ can be initially estimated by substituting v_c into Eq. (3). Inspired by a similar approach proposed by Barthel and Roux, for the effects caused by the viscoelastic energy of the EOM at different velocities in this study, the F and δ in the viscoelastic substrate can be determined while the $\Delta\gamma_{eff}$ was used to replace the $\Delta\gamma$ in the Eqs. (1) and (2) [43]. For a rigid indenter wrapped with scleral tissue, the radius is $R=r+h$, where r is the radius of the indenter and h is the thickness of the sclera. The equivalent elastic modulus of the indenter wrapped with scleral tissue and the EOM substrate becomes $E^*=\left[\left(1-\nu_{Sclera}^2\right)/E_{Sclera}+\left(1-\nu_{EOM}^2\right)/E_{EOM}\right]^{-1}$. Therefore,

$$F=\frac{4}{3}\frac{E^*a^3}{R}-\sqrt{8\pi E^*a^3\Delta\gamma_{eff}} \tag{5}$$

$$\delta=\frac{a^2}{R}-\sqrt{\frac{2\pi a\Delta\gamma_{eff}}{E^*}} \tag{6}$$

when v_c tends to 0, the above equation will change to the form applicable to quasi-static, i.e., Eqs. (1) and (2).

To make the results more generalizable, all dimensional parameters were converted to dimensionless parameters. The dimensionless forms were proposed by Lin and Violano, that is, $\hat{F} = F / \left(3\pi R \Delta\gamma_{eff}\right)$, $\hat{\delta} = \delta\left[3\pi^2 \Delta\gamma_{eff}^2 R / \left(2E^{*2}\right)\right]^{-1/3}$, $\hat{a} = a / R$, $\Delta\hat{\gamma}_{eff} = \Delta\gamma_{eff} / \left(E^* R\right)$, $\hat{F}_{pull-off} = F_{pull-off} / \left(3\pi R \Delta\gamma_{eff}\right)$, $\hat{v}_c = v_c / v^*$, and thus $\hat{V} = V / v^*$ [28, 46].

Therefore, the above relationships can be rewritten as

$$\hat{F} = \frac{4}{3}\hat{a}^3 - \sqrt{8\pi\hat{a}^3\Delta\hat{\gamma}_{eff}} \tag{7}$$

$$\hat{\delta} = \hat{a}^2 - \sqrt{2\pi\hat{a}\Delta\hat{\gamma}_{eff}} \tag{8}$$

In Eq. (7), the first term is the dimensionless Hertzian contact pressure, while the second is the dimensionless Kendall interface adhesion force.

2.4.2 Wiechert Viscoelastic Model

Most biological tissues, including the EOM, exhibit viscoelastic properties. To characterize the viscoelastic behavior of the EOM, the Wiechert model was selected [2]. This model employs a superposition of linear combinations of multiple spring-damper units (Fig. 3), allowing for the separation of transient elastic behavior from long-term viscoelastic behavior. This approach enables an accurate description of the stress-relaxation behavior of the material and facilitates the use of finite element analysis.

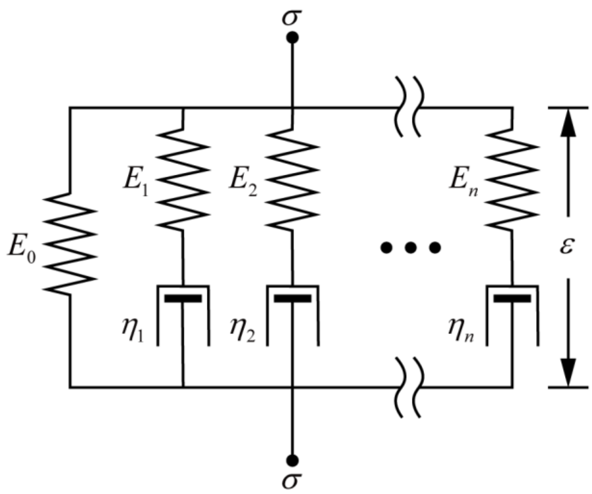

Fig. 3. Schematic diagram of the Wiechert viscoelastic model.

When utilizing the Abaqus software, it becomes essential to employ the Prony series formulation, which involves considering multiple characteristic times τ_i $\left(i=1,2,\ldots,N\right)$. In this formulation, the time-dependent relaxation modulus $E\left(t\right)$ is expressed in terms of the Prony series [47]:

$$E\left(t\right)=E_{\infty}\frac{1-\sum_{i=1}^{n}g_i\left(1-e^{-t/\tau_i}\right)}{1-\sum_{i=1}^{n}g_i} \tag{9}$$

The relaxation modulus of the EOM in the time-dependent relaxation modulus $E\left(t\right)$, normalized by the initial modulus $E_0=E_{\infty}/\left(1-\sum_{i=1}^{n}g_i\right)$, can be expressed using the Prony series $E\left(t\right)/E_0=1-\sum_{i=1}^{n}g_i\left(1-e^{-t/\tau_i}\right)$.

For the Abaqus software, when a viscoelastic model is defined in the time domain, the following parameters need to be provided as input: g_i (normalized Prony coefficients for shear behavior), k_i (normalized Prony coefficients for volumetric behavior), and τ_i (relaxation times of the Prony series). Abaqus assumes that g_i and k_i are independent of each other. In this particular study, the volume changes in the material are not taken into account, so the k_i values will be omitted [48]. The specific values for g_i and τ_i are presented in Table 3.

Table 3. The relevant parameters of the finite element model.

Model	Material model	Density	Material parameters	
Indenter	Elastic	7.85 g/cm^3	E =200 GPa, ν =0.3	
Sclera	Elastic	1.076 g/cm^3 [49]	E =11.2 kPa, ν =0.47	[This work]
EOM	Elastic Prony	1.060 g/cm^3 [50]	E =4.34 kPa, ν =0.47 g_1 =0.25, τ_1 =1.72 s g_2 =0.23, τ_2 =23.94 s g_3 =0.27, τ_3 =276.17 s	[This work]

2.5 Finite element model

Based on the experiments in the previous sections, a finite element model was constructed using the commercial Abaqus software, as illustrated in Fig. 4.a. The radius of the spherical rigid indenter is r and the thickness of the sclera is h. The total radius of the scleral tissue-wrapped indenter is $R = r + h$. The indenter was set as a rigid body according to the experiment, and then the "Tie" was used to bind the indenter to the scleral tissue. The scleral tissue was characterized by a linear elastic model, while the EOM was assumed to follow both a linear elastic constitutive model and a viscoelastic constitutive model based on the Prony series. Specific parameters are shown in Table 3. The model was created using axisymmetric four-node elements (CAX4RH). The indenter radius was set to 1 mm, and the thickness of the sclera model was assumed to equal the average experimental value of 0.55 mm. In the EOM model, the dimension along the x-axis is half the width of the experimental EOM with a size of 5 mm, and the dimension along the z-axis is the thickness of the experimental EOM with a size of 3 mm.

The descent of the indenter continued for 0.2 mm, resulting in δ of approximately 0.1 mm.

Upon reaching this value of the δ, the indenter reversed its direction of travel while adopting the bilinear cohesive zone model (CZM) depicted in Fig. 4.b [51, 52].

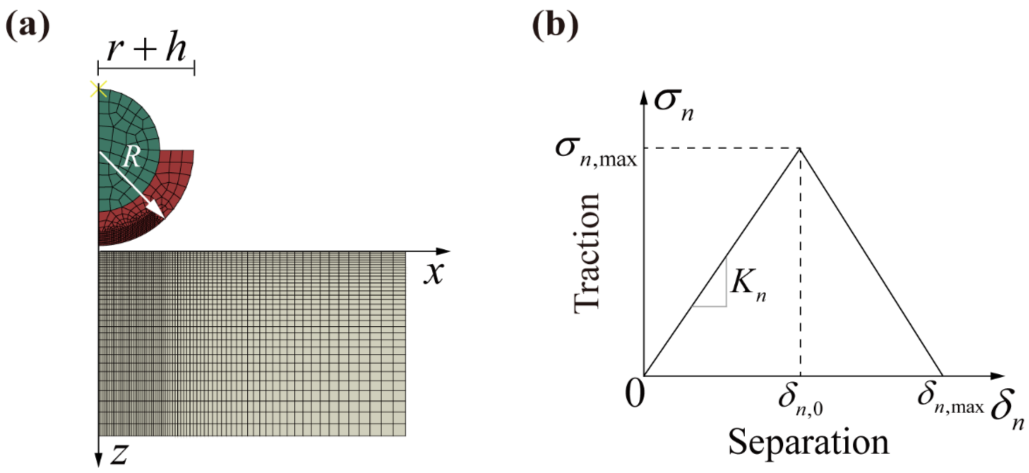

Fig. 4. Schematic diagram of the contact model between the scleral tissue-wrapped indenter and the EOM. **(a)** Finite element meshing diagram. **(b)** Model of the bilinear cohesive zone between the two contact surfaces used to simulate the finite element model.

In the finite element simulations, the scleral compressive elastic modulus in the thickness direction was derived from the results of the uniaxial compression test on porcine sclera in vitro, which are presented in Table 3. The details of this experiment are described in the Supplementary Material. The compressive elastic modulus of the EOM in the thickness direction was obtained from the indentation phase of the compressive stress-relaxation test, specifically before the relaxation occurs. This elastic modulus was determined by analyzing the experimental results using the model proposed by Sneddon and shown in Eq. (10) [53].

$$E = \frac{F\left(1-\nu^2\right)}{2a\delta}, \tag{10}$$

where F is the applied load, ν is the Poisson's ratio, a is the contact radius, and δ is the indentation displacement.

To simulate the adhesion behavior between the sclera and the EOM at different separation velocities, the unloading velocities in the finite element simulation were set to the experimental values of 0.5, 1, 6, 18, 30, and 42 mm/min, as well as eye saccade velocities of 300, 3000 and 6000 mm/min. The adhesion behavior was primarily determined by the bilinear criterion of the work of adhesion, specifically the area under the cohesion zone model curve (Fig. 4.b). However, the exact shape of the cohesive zone model has negligible influence on the overall adhesive response as long as the area under the cohesive zone model curve remains constant [54].

In this study, it was assumed that the adhesion between the scleral tissue-wrapped indenter and the EOM specimen was simultaneously and independently present in the normal and tangential directions. Under the interaction module, the cohesive behavior was selected in the contact property option. The stiffness value of K_n was set to 20 MPa/mm in the normal direction and the other two tangential directions, respectively, with the "any slave nodes experiencing contact" option.

The damage criterion adopted in the interaction module was set to "maximum separation", with values of $\delta_{n,0}$ was set to 9×10^{-5} mm. Evolution of specify damage was controlled by energy, and the fracture energy parameter was calculated using Eq. (3) to determine the equivalent work of adhesion at velocities of 300, 3000, and 6000 mm/min. At a velocity of 0.5 mm/min, the equivalent work of adhesion was set to 1.3×10^{-7} J/mm^2. Other parameter settings are shown in the Supplementary Material.

The contact area was meshed using a local seed size of 0.01 mm, while other areas of the EOM were meshed using unidirectional encrypted seeds with a minimum size of 0.01 mm and a maximum size of 0.2 mm. The sclera was also locally seeded in the contact area with a size of 0.01 mm, while other areas used global seeds with a size of 0.2 mm. When the number of elements in the finite element model was tripled, the error caused by increasing the number of elements was 3.6%. From the above results, it is indicated that the finite element meshing is reasonable and the resulting error can be accepted.

The models assumed that the nodes at the bottom boundary of the EOM were completely fixed, while the nodes on the symmetry axis were restricted in the perpendicular direction of the symmetry axis. Two analysis steps were defined for the model, both of which were defined as viscous steps. The contact and pull-off process observed experimentally between the scleral tissue-wrapped indenter and the EOM was simulated using the displacement control methods.

2.6 Eye Movement Model

During eye abduction, both the active contraction force of the LR and the passive force of MR are essential in maintaining the mechanical balance of the eye [55]. Therefore, this study focuses on calculating the active moment of the LR (M_{ac}) and the passive moment of the MR (M_{pa}) by using the traditional model and the active pulley model. The active pulley model differs from the traditional model by considering the pulley of the EOMs. Setting the center of the eye at point O as the (0, 0) point, OXYZ was defined as the stationary coordinate system, and OX′Y′Z′ was defined as the body axes system of the eye. Fig. 5.a illustrates the initial position of the key points for the LR, with the origin point M_1 (-34.00, -13.00, 0.60), tangent point T_1 (-8.12, 9.39, 0.58), pulley P_1 (-11.00, 10.02, -0.50), and insertion point I_1 (6.50, 10.08, 0.00). Similarly, the initial position of the key points for MR are M_2 (-30.00, -17.00, 0.60), T_2 (1.82, -12.30, 0.12),

P_2 (-5.00, -14.40, -0.60), and I_2 (8.42, -9.65, 0.00) [33, 55-57]. Capital letter subscripts are used to differentiate the different EOMs. The corresponding translation relations for the coordinates of the active pulley can be derived from the study of Demer et al [34]. The coordinate points on the eye before and after the eye rotation can be converted by Eq. (11).

$$\begin{bmatrix} x \\ y \\ z \end{bmatrix} = \begin{bmatrix} \cos\theta\cos\varphi & \sin\theta\cos\varphi & -\sin\varphi \\ \cos\theta\sin\varphi\sin\psi - \sin\theta\cos\psi & \cos\theta\cos\psi + \sin\theta\sin\varphi\sin\psi & \cos\varphi\sin\psi \\ \sin\theta\sin\psi + \cos\theta\sin\varphi\cos\psi & \sin\theta\sin\varphi\cos\psi - \cos\theta\sin\psi & \cos\varphi\cos\psi \end{bmatrix} \begin{bmatrix} x' \\ y' \\ z' \end{bmatrix} \tag{11}$$

Where the rotation angles θ, φ, and ψ represent the rotation angles around the OZ, OY, and OX axes, respectively. During eye abduction, the rotation angles φ and ψ are equal to 0°. The updated geometry of the LR is related to the abduction angle θ (Fig. 5.b). In the traditional model, the new tangent point S_1 was obtained by substituting the coordinates of the new insertion point I_1' and origin point M_1 into Eq. (12). In the active pulley model, the new tangent point was obtained by substituting the coordinates of the new insertion point I_1' and the new pulley P_1' into Eq. (12).

$$\begin{cases} x_T^2 + y_T^2 + z_T^2 = R_e^2 \\ x_T x_M + y_T y_M + z_T z_M = R_e^2 \\ \left(y_M z_I - z_M y_I\right) x_T + \left(y_M x_I - x_M z_I\right) y_T + \left(x_M y_I - y_M x_I\right) z_T = 0 \end{cases} \tag{12}$$

Where R_e represents the radius of the eye, with a mean value of 12.43 mm used in this study.

When the LR actively contracts, the abduction of the eye will occur. Based on the hypothesis proposed by our research group, the separation of the EOM from the sclera during eye abduction can be likened to the crack propagation in the adhesion region between the sclera and the EOM towards the muscle insertion point on the sclera. This propagation occurs at an equivalent separation angle of α, which corresponds to the eye abduction angle θ. Different eye movement velocities correspond to different velocities of crack propagation, and the separation between the sclera and the EOM occurs more rapidly during rapid eye movements. The adhesion region during eye movement is the area between the tangent points on the sclera and the EOM before and after movement. Consequently, in the JKR model, the contact arc length between the sclera and the EOM is approximatively represented by l that corresponds to the arc length between the tangent points on the sclera. Furthermore, the adhesion force between the sclera and the EOM was assumed perpendicular to $T_1'S_1$ (Fig. 5.c). The separation angle α can be approximatively described as

$$\alpha = \left(l / R_e\right) / \left(180 / \pi\right) \tag{13}$$

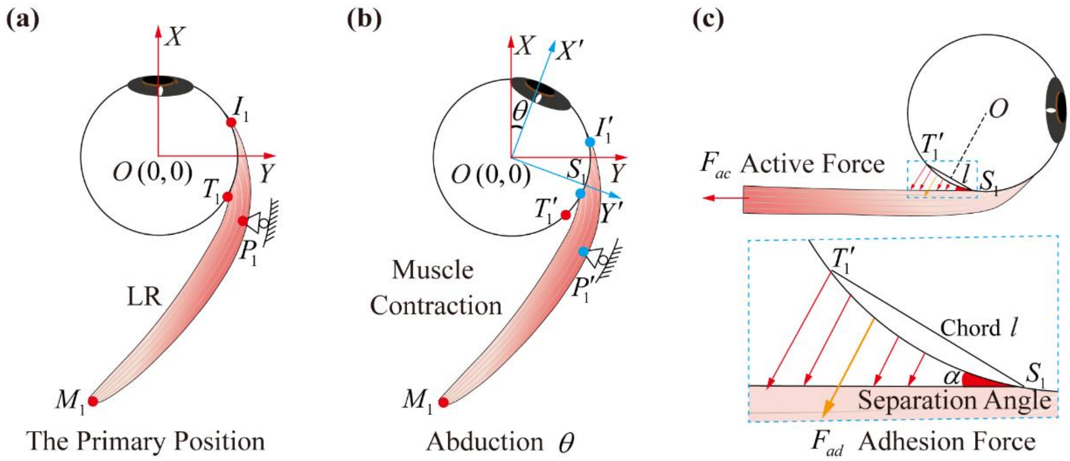

Fig. 5. Adhesion influences eye motion. **(a)** The reference coordinate system OXY depicts the primary position of the eye, where *O* represents the center of the eye, and M_1, T_1, P_1, and I_1 correspond to the origin, tangent, pulley, and insertion points of the LR, respectively. Detailed coordinates of the EOM are provided in Supplementary Material. **(b)** Schematic diagram illustrating the EOM in contact with the sclera after the abduction. The rotated coordinate system is denoted as OX'Y', with I_1, P_1, and T_1 transformed into I_1', P_1', and T_1', respectively, as the eye is rotated by an angle of θ. S_1 represents the new tangent point. **(c)** Illustration of adhesion

between the sclera and the EOM. The active force F_{ac} separates the EOM from the sclera at an angle of α, creating an adhesion region between the two separated interfaces. The resultant force within the adhesion region is denoted as the adhesion force F_{ad}. The chord l represents the distance between the old tangent point T_1' and the new tangent point S_1. The adhesion force acts perpendicular to $T_1'S_1$, and the length of the arm for the adhesion moment created by this force is approximately one-sixth of l.

The mechanical equilibrium within the intraocular system relies on the characteristics of orbital tissues and EOMs. The balance of the eye is maintained by the passive moment of MR denoted as M_{pa}, the active moment of the LR denoted as M_{ac}, the adhesive moment of the sclera and the EOM denoted as M_{ad}, and the resistive moment provided by other tissues in the orbit denoted as M_t. Based on previous studies conducted by our research group, the coordinates of each key point of the EOMs before and after eye movement are combined with the equivalent rotation angle of the eye [56, 58]. Subsequently, the force exerted by each EOM during the three-dimensional movement of the eye can be determined using Eq. (14), which governs the balance of eye movement.

$$M_{ac} - M_{ad} - M_{pa} - M_t = 0 \tag{14}$$

According to a previous study, in Eq. (14), the resistance moment $M_t = 12.43\theta K_t R_e$, the limiting stiffness K_t =1.245 mN/deg and the active moment $M_{ac} = F_{ac} \times R_e$, where F_{ac} denotes the active force of the LR [59, 60]. The adhesion moment $M_{ad} = F_{ad} \times l / 6$, where F_{ad} denotes the adhesion force. We use the maximum adhesion force (pull-off force) when calculating the adhesion moment. In addition, to calculate the effect of the adhesion moment on eye movements, we calculated the adhesion moment ratio to the total moment, which can be expressed as the ratio of M_{ad} to the summation of M_{ac}, M_{pa}, M_{ad}, and M_t.

According to the relevant literature, The formula for the passive moment is $M_{pa}=F_{pa}\times R_e$, where F_{pa} can be obtained from Eq. (15) [61].

$$F_{pa}=b\frac{A_0}{L_0^3}\Delta L^3+c\frac{A_0}{L_0^2}\Delta L^2+d\frac{A_0}{L_0}\Delta L \tag{15}$$

In Eq. (15), the MR cross-sectional area A_0 =17.4mm^2, the initial length L_0 =39.4mm, the length change $\Delta L=L-L_0$, L is the length of the MR after the corresponding eye rotation. The b, c, and d are constants, where b =23.9, c =8.4, and d =0.8, respectively [56].

2.7 Velocity Conversion Relationship

Different units of velocity were used to describe the corresponding results. The specific velocity conversion relationship is shown in Table 4.

Table 4. Velocity conversion relationship.

Unloading velocity (mm/min)	**Dimensionless velocity $\hat{V}$**	**Eye movement velocity (deg/s)**
0.5	4	0.04
1	7	0.08
6	42	0.5
18	127	1.4
30	212	2.3
42	297	3.2
300	2119	23
3000	21186	231
6000	42373	461

2.8 Statistics

The experimental data obtained in this study were presented as mean ± standard deviation (s.d.). The statistical analysis was evaluated using a one-way analysis of variance (ANOVA) subjected to an LSD test using SPSS v.26.0 (SPSS Inc., Chicago, IL, USA). For experimental groups with different velocities, Tukey's *post-hoc* test was used to distinguish the differences. A probability value (**p**) of less than 0.05 was considered indicative of statistical significance.

3. Results

3.1 Experimental results of adhesion behavior between EOMs and sclera

Fig. 6 shows the analysis of the dimensionless equivalent work of adhesion $\Delta\hat{\gamma}_{eff}$ as a function of the dimensionless unloading velocity $\hat{V}$. The figure shows the indenter radius and the average contact radius. The results show that $\Delta\hat{\gamma}_{eff}$ is velocity dependent at contact radii at the sub-millimeter level with an indenter radius of 1 mm. With an indenter radius of 1.5 mm, the contact radius is between sub-millimeter and millimeter-level thresholds, and $\Delta\hat{\gamma}_{eff}$ is some velocity dependent. In addition, the results showed that there is velocity dependence between quasi- and non-quasi-static velocities (e.g., $\hat{V}$ =212 and $\hat{V}$ =297), regardless of whether the contact radius is sub-millimeter or millimeter. In the subsequent analysis, we took the case with the indenter radius of 1 mm as an example.

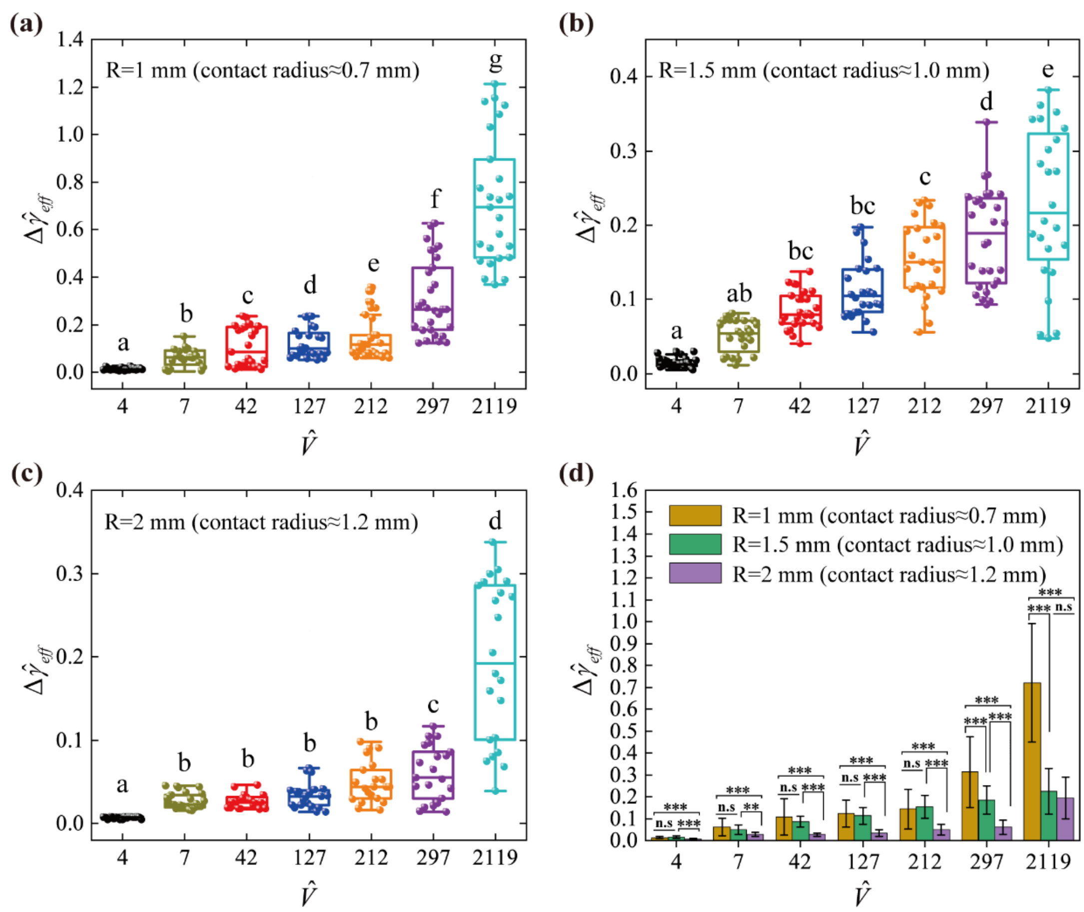

Fig. 6. Analysis of the dimensionless equivalent work of adhesion $\Delta\hat{\gamma}_{eff}$ as a function of the dimensionless unloading velocity $\hat{V}$. The experimental data and their dispersion are presented through box plots. $\Delta\hat{\gamma}_{eff}$ were measured at each $\hat{V}$ using a one-way ANOVA (** indicates **p** < 0.01 and *** indicates **p** < 0.001, respectively; and signed by **n.s** indicate no statistical differences among the groups with **p** > 0.05). Differences between values with different lowercase letters were significant (**p** < 0.05). Identical letters on the same box plots are statistically similar. The figure represents experimental results with an indenter radius of **(a)** 1mm (contact radius is 0.7 mm), **(b)** 1.5mm (contact radius is approximately 1.0 mm), and **(c)** 2mm (contact radius is approximately 1.2 mm). **(d)** Significance analysis of different radius indenter.

To enhance the generalizability of the results, all important parameters were transformed into dimensionless parameters. Fig. 7 illustrates the experimental dimensionless contact line velocity

$\hat{v}_c$ plotted against the relative increase in the work of adhesion $\left(\Delta\gamma_{eff} - \Delta\gamma\right)/\Delta\gamma$. The best fit trend curve by Eq. (3), whose parameters were n = 0.368 and v^* = 0.00236 mm/s, will then be normalized, indicated by the red line. The results demonstrate a correlation between $\left(\Delta\gamma_{eff} - \Delta\gamma\right)/\Delta\gamma$ and $\hat{v}_c$, suggesting that the velocity dependence cannot be neglected in considering the adhesion of viscoelastic materials.

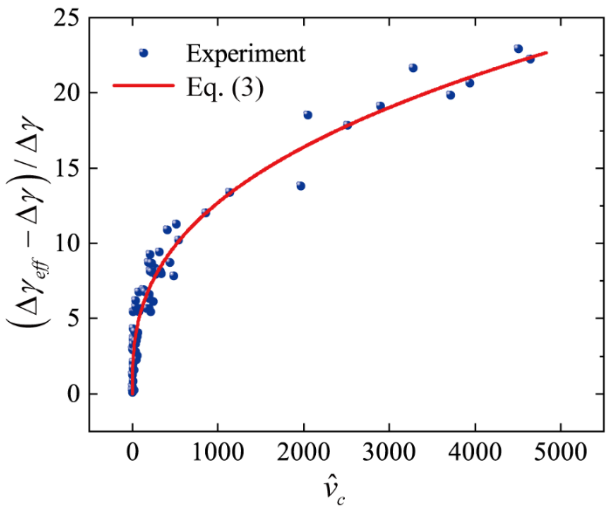

Fig. 7. Experimental dimensionless contact line velocity $\hat{v}_c$ versus relative increase in the work of adhesion $\left(\Delta\gamma_{eff} - \Delta\gamma\right)/\Delta\gamma$. The blue dots were obtained from the experimental contact radius a, while the red line was theoretical predictions based on Eq. (3), where the parameters of the fitted curve are chosen as n = 0.368 and v^* = 0.00236 mm/s.

In addition to the aforementioned results, the adhesion behavior of the EOM was examined under various durations of air exposure, with a velocity of 0.5 mm/min. The analysis revealed no significant difference (**p** > 0.05) between the specimen groups exposed to air for 15 and 30 minutes (Fig. 8).

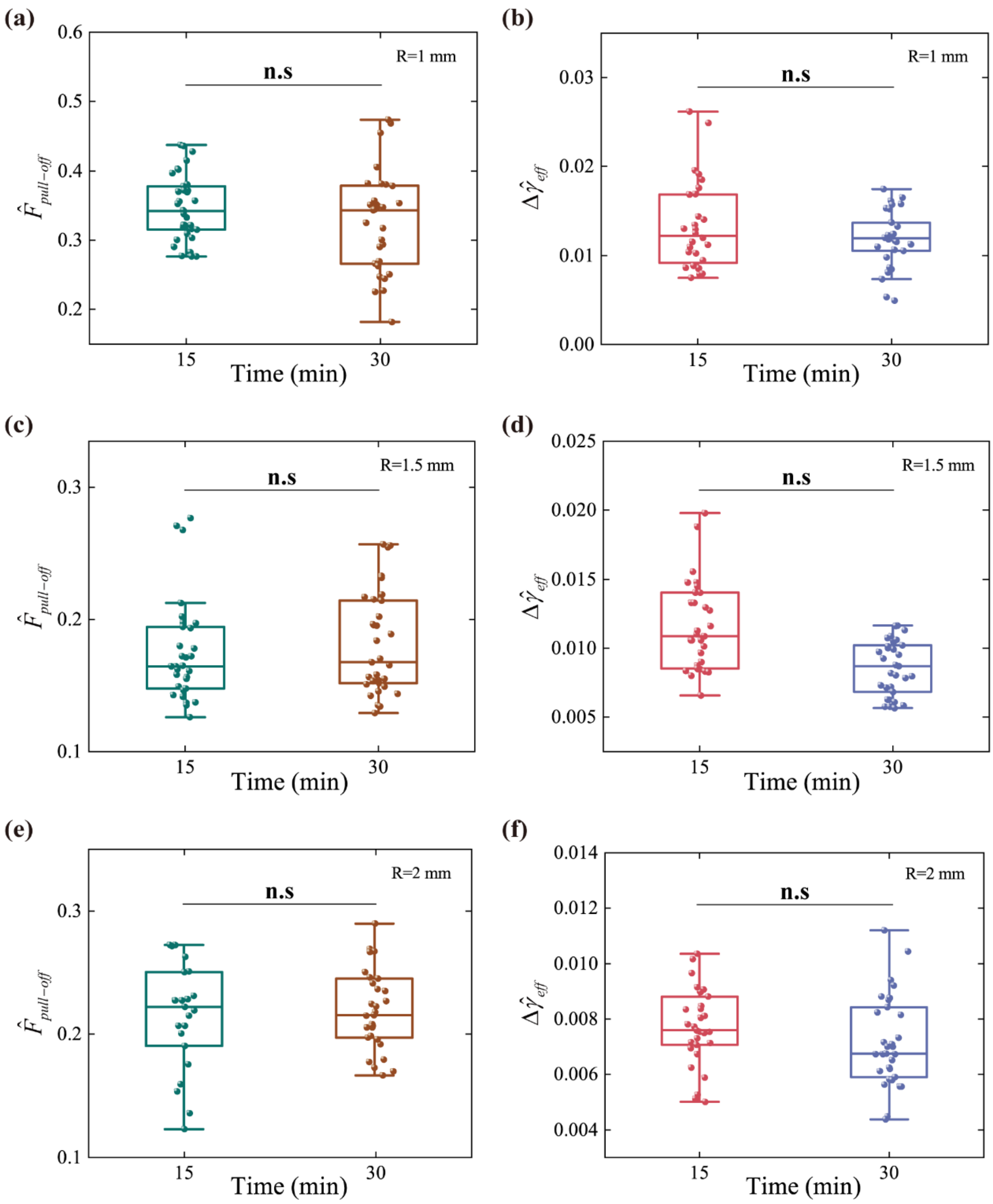

Fig. 8. The relationship between dimensionless pull-off force $\hat{F}_{pull-off}$ and exposure times of EOM and the relationship between equivalent work of adhesion $\Delta\hat{\gamma}_{eff}$ and exposure times of EOM. The radius of the indenter is labeled in the upper right corner of each figure. (The **n.s** indicates no statistically significant difference between groups, representing **p** > 0.05).

3.2 Numerical estimations of adhesion behavior between EOMs and sclera

3.2.1 Model validation

The finite element setup was the same as in the experiments. The finite element results were compared with the experimental results to validate models. Fig. 9.a illustrates the relationship between the dimensionless penetration depth $\hat{\delta}$ and adhesion force $\hat{F}$ for the tests at various velocities ($\hat{V}$ =4, 7, 42, 127, 212, 297, and 2119), while Fig. 9.b displays the relationship between $\hat{\delta}$ and $\hat{F}$ obtained using the finite element simulations at different velocities. The force-displacement curves during unloading differ from those during loading due to viscoelastic energy dissipation during the separation of the sclera from the EOM. As the unloading velocity increases, the pull-off force between the sclera and EOM increases, along with an increase in the pull-off force corresponding to the separation displacement. From Fig. 9.a, it is observed that dimensionless pull-off force $\hat{F}_{pull-off}$ increases by 135% when $\hat{V}$ increases from 4 to 212 in the experiments. Moreover, when $\hat{V}$ increases from 212 to 297, the corresponding increase in $\hat{F}_{pull-off}$ is 18%. As $\hat{V}$ further increases from 297 to 2119 (614% increase), $\hat{F}_{pull-off}$ only increases by 37%.

Fig. 9.b also shows that in the finite element simulation, as $\hat{V}$ increases from 4 to 212, $\hat{F}_{pull-off}$ increases by 166%. Similarly, when $\hat{V}$ increases further from 212 to 297, the corresponding increase in $\hat{F}_{pull-off}$ is 7%, which is similar to the increase observed experimentally. According to the FEM prediction, when $\hat{V}$ increases from 297 to 2119 (614% increase), $\hat{F}_{pull-off}$ only increases by 23%. A further inspection of the $\hat{\delta}$ - $\hat{F}$ behavior obtained numerically and

experimentally shows trend consistency in most values considered of $\hat{V}$, Fig. 9.

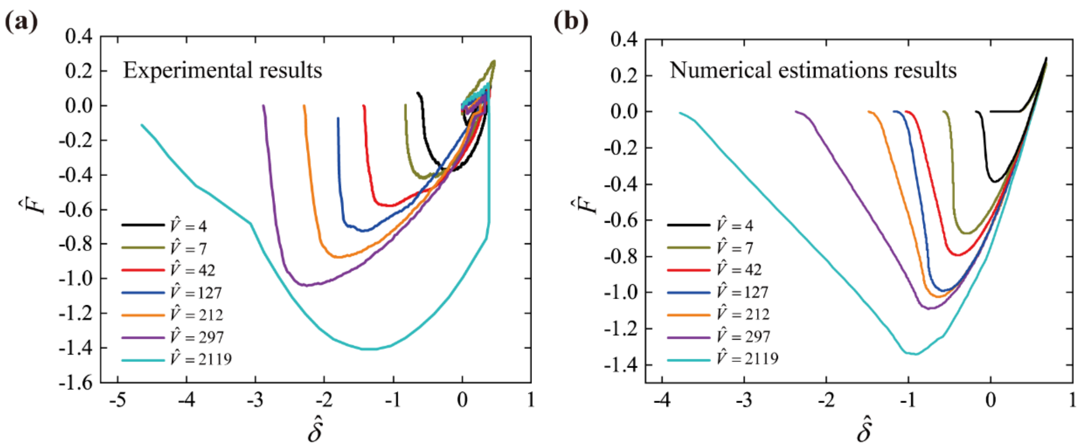

Fig. 9. Model validation of adhesion behavior between sclera and EOM at different unloading velocities. **(a)** Contact and pull-off test of dimensionless indentation displacement $\hat{\delta}$ and adhesion force $\hat{F}$ curves between the sclera and EOM at different unloading velocities, where the different color curves correspond to $\hat{V}$ =4, 7, 42, 127, 212, 297, and 2119. **(b)** Finite element simulation of $\hat{\delta}$ and $\hat{F}$ profiles between the sclera and EOM at different unloading velocities.

3.2.2 Numerical estimations results

In this section, finite element results on the adhesion between the sclera and the EOMs were presented. A loading scheme, resembling the experimental setup, was implemented in the finite element model. The nephograms of normal stress corresponding to $\hat{V}$ =42 were selected for visual representation (Fig. 10). The deformation pattern of the EOM model is very similar to the experimentally captured images.

The analysis involved four steps:

(i) Initially, the axisymmetric scleral tissue-wrapped indenter gradually approached the EOM. At this stage, the two interfaces were not in contact, resulting in no generation of normal stress on the surface of the EOM.

(ii) The indenter was then pressed to a predefined maximum value of 0.1mm, leading to the generation of the maximum negative normal stress on the EOM.

(iii) While maintaining the contact area, the indenter was lifted upwards at different velocities. This means that the previously contacted area was not allowed to separate until the pull-off force was reached. Once the pull-off force was reached, the separation of the EOM from the scleral interface began.

(iv) The indenter continued to be lifted until the two surfaces were completely separated. However, due to the viscoelastic nature of the EOM substrate, residual stresses persisted for some time even after the separation was achieved.

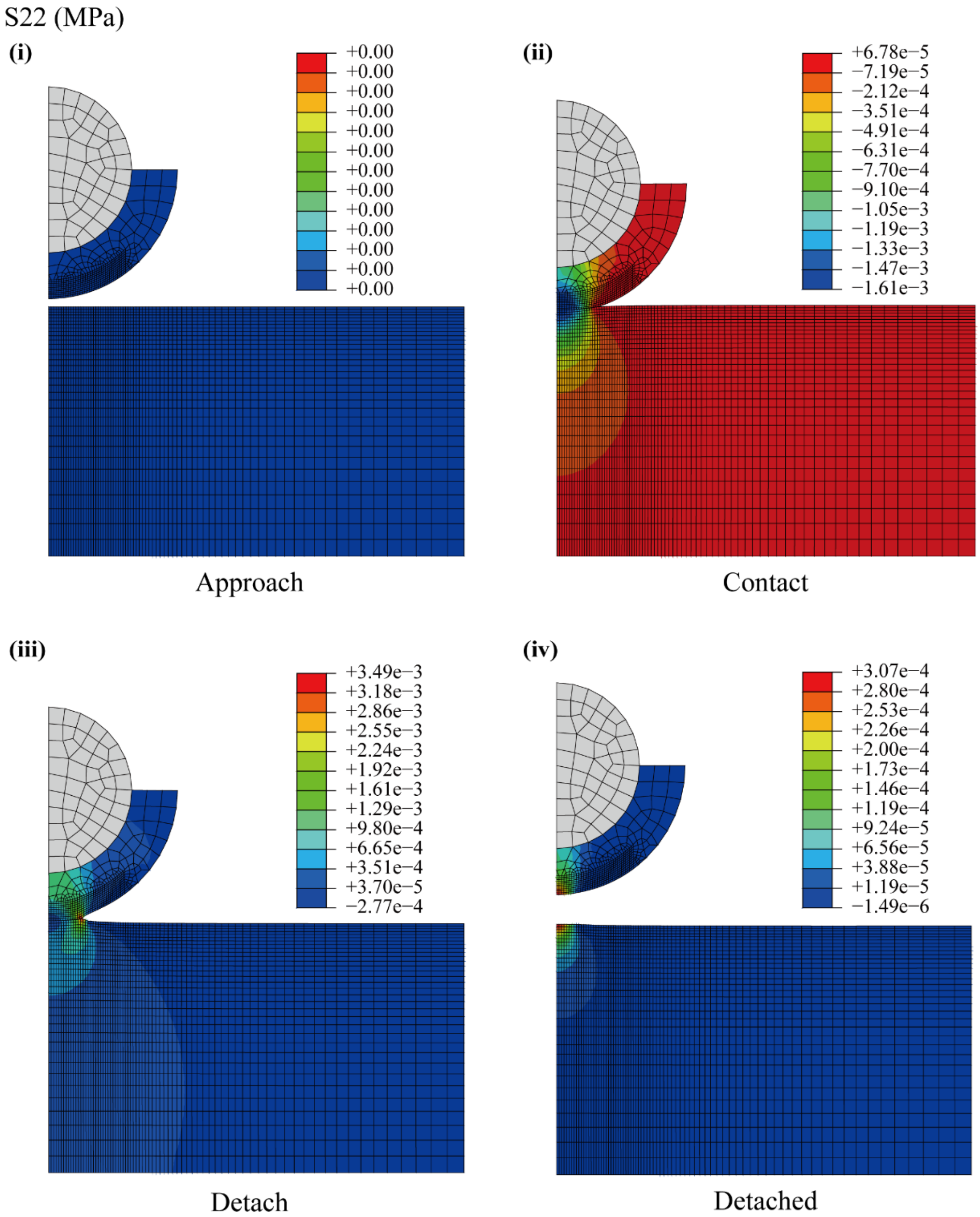

Fig. 10. Normal stress results for the EOM near the contact area in each stage of the finite element simulation, showing only the results for the axisymmetric system in the x-z plane.

Fig. 11 shows the contact stress pressure distribution between the sclera and the EOM at different phases of loading and unloading. Fig. 11.a illustrates the dimensionless force-displacement curve between the sclera and the EOM. Fig. 11.b presents the normalized stress distribution on the surface of the EOM, with the horizontal axis representing r / R_{eff} and the vertical axis representing the normalized normal stress $\sigma_n / \sigma_{n,\max}$. The phases of loading and unloading represented by the roman numerals in Fig. 11.a and Fig. 11. b correspond to each other. The $\sigma_{n,\max}$ is observed at the edge of the contact region between the sclera and the EOM, with a value of 3.49$\times$10^{-3} MPa. Fig. 11.b reveals that as the interface gradually separates, the maximum normal stress shifts from the edge towards the center of the contact area. The stress distribution on the EOM surface aligns with the findings from previous finite element simulations and is consistent with the assumptions of classical theory [12, 31].

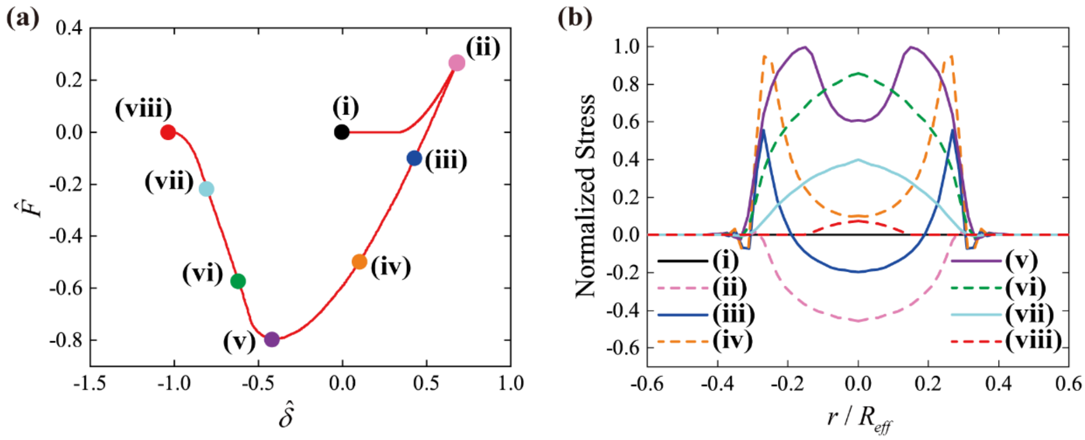

Fig. 11. Analysis of the results of the adhesion behavior between the sclera and the EOM. **(a)** Dimensionless adhesion force-displacement plots for specimens with an unloading velocity of 6 mm/min in the experiment, in which the roman serial numbers indicate the different stages of the adhesion process in the finite element simulation. **(b)** The contact pressure distribution over the contact area of the EOM at different stages of the finite element simulation.

Fig. 12.a illustrates the relationship between $\hat{\delta}$ and $\hat{F}$ for the finite element simulations at different velocities, which additionally predict velocities of $\hat{V}$ = 2119, 21186, and 42373. From the figure, it is evident that as $\hat{V}$ increases from 2119 to 42373 (1900% increase), $\hat{F}_{pull-off}$ increases 51% times, indicating a relatively inconsiderable increase. Fig. 12.b presents the variation of the experimental and finite element $\hat{F}_{pull-off}$ with $\hat{V}$. Box line plots show the

experimental data and their scattering, and big red dots indicate the finite element results using the average work of adhesion calculated by Eq. (3) as the input parameter.

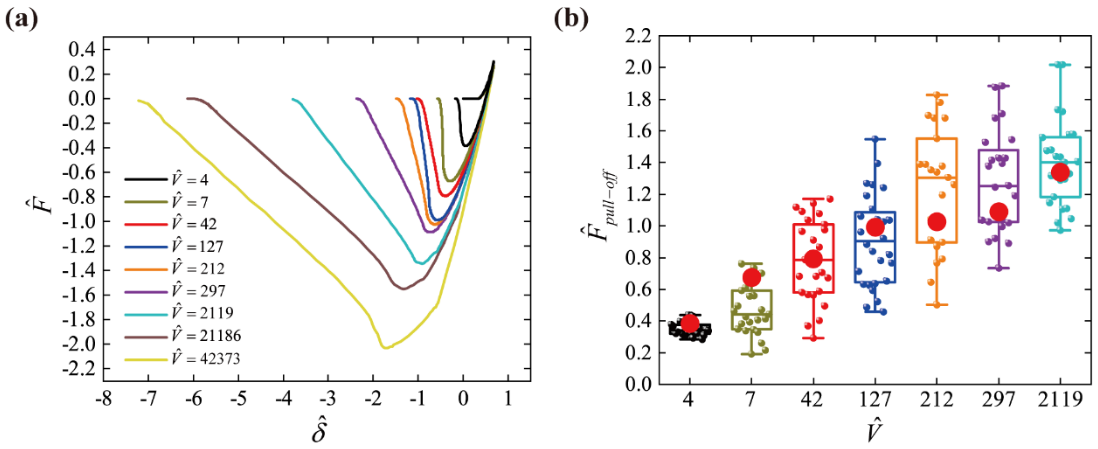

Fig. 12. Analysis of adhesion behavior between sclera and EOM at different unloading velocities. **(a)** Finite element simulation of dimensionless indentation displacement $\hat{\delta}$ and adhesion force $\hat{F}$ curves between the sclera and EOM at different unloading velocities, where the different color curves correspond to $\hat{V}$ =4, 7, 42, 127, 212, 297, 2119, 21186, and 42373. **(b)** Variation of experimental and finite element dimensionless pull-off force $\hat{F}_{pull-off}$ with dimensionless unloading velocity $\hat{V}$. Box line plots show the experimental data and their scattering, and big red dots indicate the finite element results using the average work of adhesion calculated by Eq. (3) as the input parameter.

3.3 Biomechanical properties of the EOM along the thickness direction

The force-displacement curves obtained from compressive stress-relaxation tests conducted on the EOM along the thickness direction are presented in Fig. 13.a, and the plot of normalized relaxation modulus against time is depicted in Fig. 13.b. The mean value is represented by the red line, while the shaded region corresponds to the standard deviation of measurements. The elasticity modulus of the EOM along the thickness direction was determined through fitting using Eq. (10), resulting in a value of 4.34 ± 2.34 kPa (average fit $R^2 = 0.934$).

To generate data applicable in the finite element software Abaqus, the Prony series was fitted to the normalized relaxation modulus curves (Fig. 13.c). The parameters of the second-order Prony series (curve fit $R^2 = 0.989$) were obtained as follows: g_1 =0.40, τ_1 =5.39s, g_2 =0.30, τ_2 = 156.60s. Additionally, the parameters of the third-order Prony series (curve fit $R^2 = 0.999$) were determined as follows: g_1 =0.25, τ_1 =1.72s, g_2 =0.23, τ_2 =23.94s, g_3 =0.27, and τ_3 =276.17s. The above material parameters are organized in Table 3. Fig. 13.c shows the results of the least squares regression method used to fit the EOM specimens to the Prony series at a 10% strain level, indicating that the third-order Prony series provides a better fit.

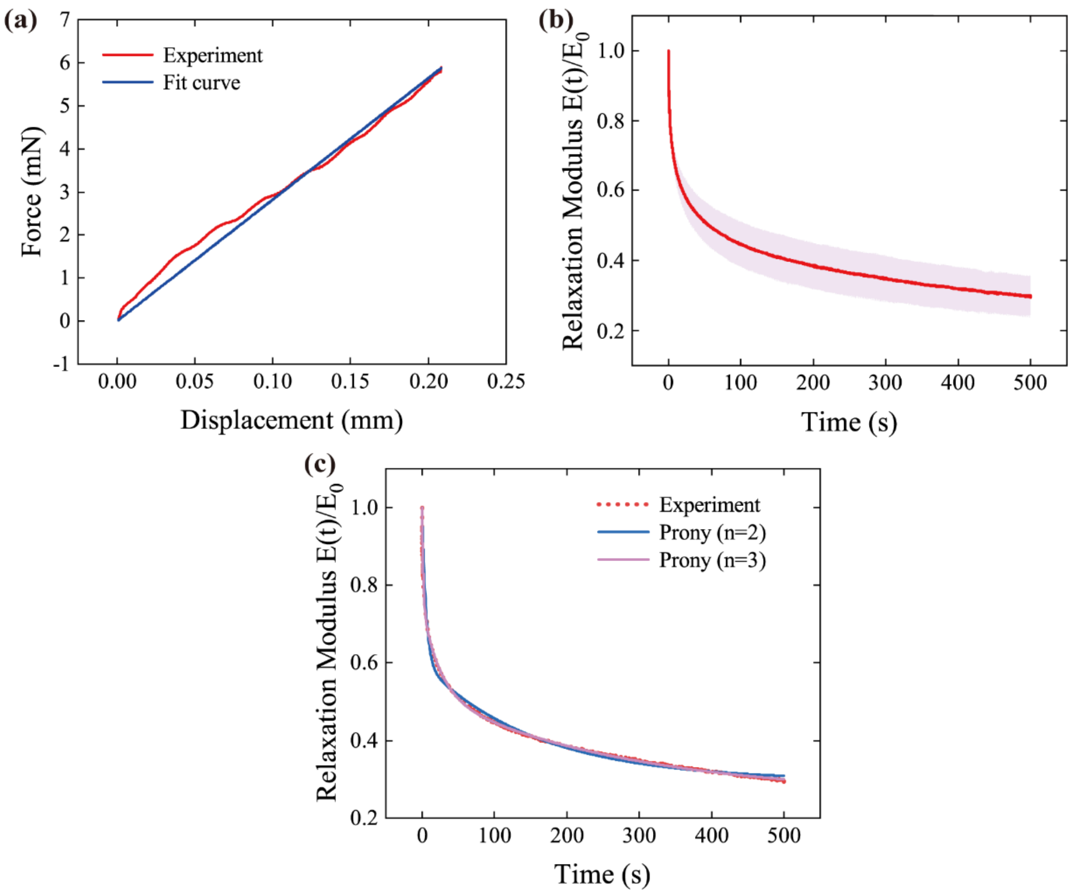

Fig. 13. Analysis of EOM compressive stress-relaxation tests. The red line represents the mean

value of the experimental curve, and the shaded area indicates the standard deviation. **(a)** Compressive stress-relaxation tests were conducted on EOM specimens along the thickness direction. **(b)** Variation of normalized relaxation modulus with time for EOM specimens at a 10% strain level. **(c)** Least-squares regression fitting of Prony series to EOM specimens at a 10% strain level.

3.4 Adhesion moment

Through the calculation of the equilibrium equation of eye motion, it becomes evident that the separation angle α exhibits a linear increase with the increment of the eye abduction angle θ (Fig. 14.a). The results show the adhesion moments for the traditional model and the active pulley model, as well as the adhesion moment ratio to the total moment for both models. The adhesion moment also shows an increase in correlation with both the eye abduction angle and the velocity of separation of the EOM from the sclera (Fig. 14.b and Fig. 14.c). Additionally, the adhesion moment between the sclera and the EOM experiences an augmentation as the eye undergoes abduction, resulting in a corresponding rise in the adhesion moment ratio to the total moment (Fig. 14.d and Fig. 14.e). In the traditional model, the adhesion moment ratio to the total moment was 0.002% to 0.01% at V =0.04 deg/s for eye abduction angles within the range of 5° to 35°. However, the adhesion moment ratio to the total moment in the range of 5° to 35° of eye abduction was approximately 0.08% to 0.53% when V =461 deg/s. The maximum adhesion moment increased from 0.76 mN·mm to 36.2 mN·mm. In the active pulley model, the adhesion moment ratio to the total moment was 0.002% to 0.01% at V =0.04 deg/s for eye abduction angles within the range of 5° to 35°. However, the adhesion moment ratio to the total moment in the range of 5° to 35° of eye abduction was approximately 0.09% to 0.50% when V =461 deg/s. The maximum adhesion moment increased from 0.83 mN·mm to 33.8 mN·mm.

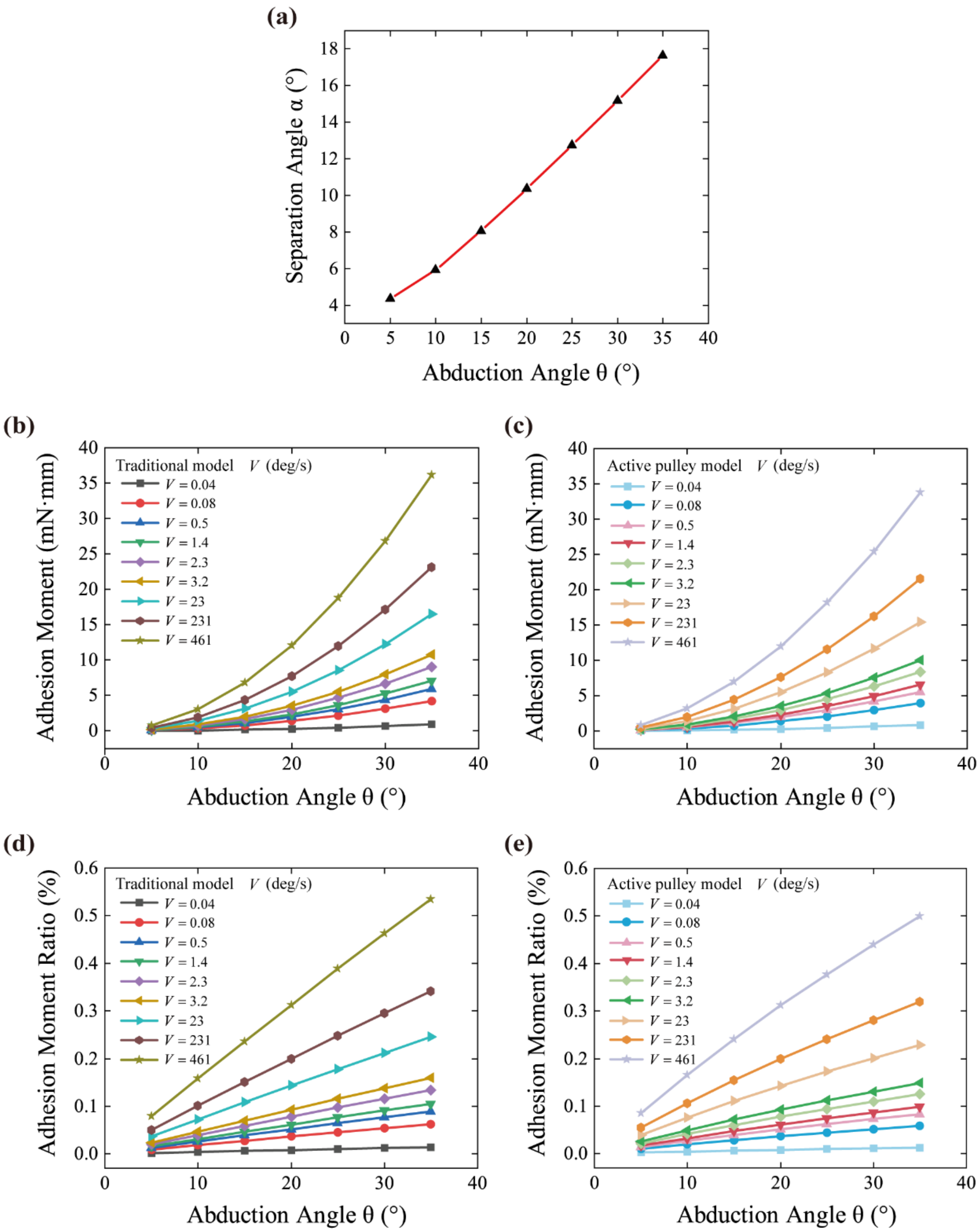

Fig. 14. Analysis results of the adhesion moment between the sclera and the EOM. **(a)** Relationship between the separation angle α of the sclera and the EOM and the abduction angle θ. Relationship between the adhesion moment and the abduction angle θ for different velocities

of the sclera and EOM separation in **(b)** traditional model and **(c)** active pulley model. Relationship between the percentage of adhesion moment and the abduction angle θ at different velocities of the sclera and EOM separation in **(d)** traditional model and **(e)** active pulley model.

4. Discussion

Previous studies often neglected the contact behavior between the sclera and the EOMs. However, the adhesion behavior between the scleral tissue-wrapped indenter and the EOMs was observed in the contact and pull-off tests conducted in this paper. The adhesion force-displacement trend of EOM-scleral tissue adhesion (Fig. 9.a) aligns with the adhesion force-displacement curve observed in facial adhesion experiments conducted by Dai et al. [9]. According to Muller's description, the pull-off force varies with the unloading velocity, with higher unloading velocities resulting in higher pull-off forces [22]. Moreover, the area enclosed under the force-displacement curve increases as the unloading velocity increases, indicating that the work of adhesion also increases with the unloading velocity.

Furthermore, contact and pull-off tests were performed using indenters with radii of 1 mm, 1.5 mm, and 2 mm at various unloading velocities (Fig. 6). In a previous study, it was also observed that variations in indenter radius at the sub-millimeter and millimeter levels caused differences in the work of adhesion [62]. This sensitivity of the sub-millimeter contact radius to size may be the source of the difference in results. In addition to the differences caused by indenter size, between quasi-static and non-quasi-static velocities, the dimensionless equivalent work of adhesion $\Delta\hat{\gamma}_{eff}$ for the indenters is also statistically different. Therefore, if adhesion behavior under the high eye movement velocity is to be considered, the viscoelasticity of the tissue should be taken into account.

To investigate the impact of the duration of EOM exposure to air on adhesion behavior, experiments were performed with different exposure times. Clinicians typically perform EOM surgery for approximately 30 minutes [63]. The exposure time was divided into 15-minute and 30-minute groups, and the results in Fig. 8 showed no significant differences between these two groups.

In combination with the results of the experiments and the finite element model in this study, it was observed that the pull-off force between the sclera and the EOM gradually increased with the increase of unloading velocities (Fig. 9). However, the rate of increase in the pull-off force diminished at higher unloading velocities. Despite the different materials studied, Jiang et al. found similar trends in their finite element simulations of contact between viscoelastic stamps and spherical transfer elements [30]. Han et al. effectively revealed the adhesion rates of articular cartilage tissues at various unloading velocities through experimental studies [21]. Naraghi et al. report a simple method for extending the range of controlled adhesion of a stamp, which can be achieved by adjusting the thickness of the elastic layer and the separation rate [64]. Das et al. conducted a comprehensive investigation on the adhesion behavior of polyacrylonitrile nanofibers, focusing specifically on its dependence on the velocity of unloading [65]. Their findings revealed a consistent and progressive improvement in the apparent adhesion as the unloading velocity increased. These findings are in line with the results obtained in this study.

In this study, we determined the elastic modulus and viscoelastic parameters of the EOMs along the thickness direction through compressive stress-relaxation tests. When the EOMs regulate eye movements by active contraction and passively stretched, and the force direction of the EOM is mainly along the length direction. For this reason, many scholars have focused on the tensile elastic modulus of the EOM along the length direction, for example, Jeong et.al set the elastic modulus of the EOMs to 0.09 MPa in finite element modeling [66]; Schutte et al. used a value of 40 kPa as the elastic modulus of the EOMs input into the finite element model [60]. The EOM wraps around the eyeball, causing the EOM and sclera to squeeze against each other. Therefore, the elastic modulus of the EOM along the thickness direction is particularly important in analyzing the adhesion between the sclera and the EOMs in this work. Up to now, there are few reports about the compressive modulus of the EOM. Therefore, the compressive modulus of the EOMs was tested in this study and was found to be 4.34 kPa.

When considering the viscoelastic properties of the EOM itself, there are two fundamental linear viscoelastic modeling approaches: the Maxwell model and the Voigt model [67]. The Maxwell model predicts relaxation behavior and describes how a material returns to equilibrium after being deformed by external disturbances. However, it is unable to accurately predict creep, which refers to the tendency of a material to undergo permanent deformation under a constant force. On the other hand, the Voigt model effectively describes creep but is less proficient in predicting relaxation [2]. Nonetheless, neither of these models adequately captures the viscoelastic properties of the EOMs. To address these limitations, we ultimately opted for the Wiechert model, which is constructed as a linear combination of multiple springs and buffers, offering a more comprehensive representation of the EOM’s viscoelastic behavior.

The elastic modulus of the sclera has been reported a lot recently, but not what was needed in this study. Many researchers focused on the tensile elastic modulus of the sclera. For example, Nguyen et.al measured the tensile modulus of the human sclera to be 2.5 MPa in 2020 [68]. In

2021, Park et.al found that the tensile elastic modulus of the human sclera varied in the anterior, equatorial, and posterior portions of the sclera, which resulted in a tensile modulus of approximately 30.8 MPa in the anterior sclera, 17.7 MPa in the equatorial portion of the sclera, and 13.3 MPa in the posterior portion of the sclera [69]. In the same year, Hatami-Marbini et al. reported that the equilibrium tensile modulus of the porcine sclera was 3-7 MPa [70]. Although several researchers had also measured the compressive elastic modulus of the sclera along the thickness, not about the sclera between the anterior and equatorial position of the eye, mainly studying the posterior sclera. For example, in 2009, Mortazavi et.al determined the compressive modulus of the human and porcine peripapillary sclera to be 1.1 kPa and 3.9 kPa, respectively [71]. In 2014, Worthington et al. measured the compressive modulus of the posterior porcine sclera to be approximately 35 kPa [72]. In 2021, Brown et al. derived from unconfined compression experiments that the average compressive stiffness of the porcine sclera near the optic nerve head was 10 kPa [73]. The scleral compressive modulus between the anterior and equatorial portions measured in this study was approximately 11.2 kPa, which is in the same order of magnitude as previously reported compressive moduli.

In this study, a 2D axisymmetric finite element model was developed to simulate the interaction between a scleral tissue-wrapped indenter and the EOM. The model considered the viscoelastic properties of the substrate and employed the JKR-like viscoelastic model to calculate the equivalent work of adhesion in the 2D simulation. However, it should be noted that the JKR-like viscoelastic model assumes the substrate to be a half-space, whereas the EOM is not of infinite thickness. To address this, we set a very small indentation displacement and concluded, based on Shull’s description of finite thickness, that the substrate thickness does not significantly impact the experimental results under the conditions of this study [74].

By comparing the finite element results with the experimental data, it is found that the dimensionless indentation displacement $\hat{\delta}$ and adhesion force $\hat{F}$ of both have the same trend. The dimensionless pull-off force $\hat{F}_{pull-off}$ of finite element calculations were within the range of experimental scatter, confirming the accuracy of the model in describing the interfacial bond and the viscoelastic properties of the EOM (Fig. 12.b).

In this study, the approximation of the indenter's unloading velocity was based on the separation velocity between the sclera and the EOM. This unloading velocity was then utilized to determine the magnitude of the equivalent work of adhesion, which was subsequently incorporated into the equilibrium equation of eye movement to calculate the adhesion moment (Fig. 14.b and Fig. 14.c). The analysis aimed to assess the impact of the adhesion moment on eye movement.

Since there is no previous report about the in vivo measurement of the adhesion behavior between the LR and the sclera, we chose to verify the active force of the LR. Collins et al. measured the active force of the LR in humans during surgery and reported values of 316.5 mN when the right eye was abducted at an angle of 15° and 487.4 mN at 30° of eye abduction [59]. In our study, the calculated active force of the LR at quasi-static velocities was within the range of 234.8 mN to 236.9 mN at 15° of eye abduction and 473.9 mN to 482.4 mN at 30° of eye abduction. The consistency between our calculated values and the previous reports verifies the accuracy of our results.

In this paper, several limitations need to be addressed in future studies. Firstly, due to the difficulty in obtaining human tissues, parameters obtained from porcine eyes were used to analyze the human oculomotor model. This results in a potential bias in the obtained results.

Furthermore, it is important to acknowledge that the adhesion area between the sclera and the EOM contains other tissues such as body fluids and fat in actual oculomotor processes. These additional factors may potentially influence the measurement of adhesion work and could be considered in future investigations. Additionally, in the finite element modeling process, a 2D axisymmetric model was used to improve the computing efficiency.

Lastly, for the contact and pull-off tests, we used in vitro EOMs. However, in the physical situation, the muscle would remain active and the muscle tension would counteract some of the adhesion forces. Also, the dryness and humidity of the muscle differed from the in vitro conditions. The adhesive behavior between the sclera and the EOM in the physical situation is not fully understood and requires further study.

Addressing these shortcomings will contribute to a more comprehensive understanding of the oculomotor system and the adhesion behavior between the sclera and the EOM in realistic physiological conditions.

5. Conclusion

During eye movements, adhesion between the sclera and the EOMs occurs. This study aimed to understand the adhesion between the porcine sclera and the EOMs at different velocities. At the saccade velocities, the adhesion moment was found to be 0.53% and 0.50% of the total moment based on the traditional and active pulley models, respectively. Although the adhesion effect is increasing at high eye movement velocities, the effect on eye movements remains minimal. According to the results of the study, the effect of adhesions between the sclera and the EOMs on eye movement can be ignored. Knowledge of the adhesion behavior between the sclera and the EOMs can supplement a portion of the unknown quantities in the equations of eye movement, resolving the contradiction between the number of equations and the mismatch of unknown quantities. Furthermore, when this adhesion behavior is considered in eye modeling, it can be ignored, thus simplifying the model reasonably well.

Declaration of Competing Interest

The authors declare that they have no known competing financial interests or personal relationships that could have influenced the work reported herein.

Author Statement

Hongmei Guo: Conceptualization, Investigation, Writing-review & editing, Funding acquisition, Supervision, Project administration. **Yunfei Lan**: Formal analysis, Investigation, Writing-original draft, Visualization, Software, Methodology. **Zhipeng Gao**: Resource, Funding acquisition, Methodology. **Chenxi Zhang**: Investigation, Software. **Liping Zhang**: Formal analysis, Investigation. **Jianying Lin**: Supervision. **Xiaona Li**: Investigation, Funding acquisition. **Ahmed Elsheikh**: Writing-review & editing. **Weiyi Chen**: Supervision, Funding acquisition.

Acknowledgment

The authors would like to acknowledge funding from the National Natural Science Foundation of China (Grants: 11802196, 31800789, 12172243, 12072218).

References

[1] L. Yoo, J. Reed, A. Shin, J.L. Demer, Atomic force microscopy determination of Young's modulus of bovine extra-ocular tendon fiber bundles, J. Biomech. 47(8) (2014) 1899-1903.

[2] A. Shin, L. Yoo, J.L. Demer, Viscoelastic Characterization of Extraocular Z-Myotomy, Invest. Ophthalmol. Vis. Sci. 56(1) (2015) 243-251.

[3] L.K. McLoon, A. Vicente, K.R. Fitzpatrick, M. Lindstrom, F.P. Domellof, Composition,

Architecture, and Functional Implications of the Connective Tissue Network of the Extraocular Muscles, Invest. Ophthalmol. Vis. Sci. 59(1) (2018) 322-329.
[4] L. Yoo, H. Kim, V. Gupta, J.L. Demer, Quasilinear Viscoelastic Behavior of Bovine Extraocular Muscle Tissue, Invest. Ophthalmol. Vis. Sci. 50(8) (2009) 3721-3728.
[5] L. Yoo, H. Kim, A. Shin, V. Gupta, J.L. Demer, Creep Behavior of Passive Bovine Extraocular Muscle, J. Biomed. Biotechnol. 2011 (2011) 526705.
[6] T. Negishi, K. Ito, A. Kamono, T. Lee, N. Ogihara, Strain-rate dependence of viscous properties of the plantar soft tissue identified by a spherical indentation test, J. Mech. Behav. Biomed. Mater. 102 (2020) 103470.
[7] S. Kalyanam, K.S. Toohey, M.F. Insana, Modeling biphasic hydrogels under spherical indentation: Application to soft tissues, Mech. Mater. 161 (2021) 103987.
[8] K.L. Johnson, J.A. Greenwood, An Adhesion Map for the Contact of Elastic Spheres, J. Colloid Interface Sci. 192(2) (1997) 326-333.
[9] A.N. Dai, W. He, S.B. Wang, W.J. Chen, C.W. Li, Z.Y. Wang, L.A. Li, In vivo adhesive behavior of human facial skin by a modified indentation test, J. Mech. Behav. Biomed. Mater. 92 (2019) 172-178.
[10] D.K. Zhu, Y.P. Liu, J.L. Gilbert, Micromechanical measurement of adhesion of dehydrating silicone hydrogel contact lenses to corneal tissue, Acta Biomater. 127 (2021) 242-251.
[11] C.X. Zhang, Y.F. Lan, H.M. Guo, Z.P. Gao, J. Song, W.Y. Chen, The adhesion behavior of the retina, Exp. Eye Res. 233 (2023) 109541.
[12] K.L. Johnson, K. Kendall, A.D. Roberts, D. Tabor, Surface energy and the contact of elastic solids, Proc. R. Soc. A 324(1558) (1971) 301-313.
[13] K. Kendall, The adhesion and surface energy of elastic solids, J. Phys. D: Appl. Phys. 4(8) (1971) 1186.
[14] K. Kendall, Thin-film peeling-the elastic term, J. Phys. D: Appl. Phys. 8(13) (1975) 1449.
[15] D. Tabor, Surface Forces and Surface Interactions, in: M. Kerker, A.C. Zettlemoyer, R.L. Rowell (Eds.), Plenary and Invited Lectures, Academic Press1977, pp. 3-14.
[16] Z. Song, K. Komvopoulos, Adhesion-induced instabilities in elastic and elastic–plastic contacts during single and repetitive normal loading, J. Mech. Phys. Solids 59(4) (2011) 884-897.
[17] D. Baek, P. Hemthavy, S. Saito, K. Takahashi, Evaluation of energy dissipation involving adhesion hysteresis in spherical contact between a glass lens and a PDMS block, Appl. Adhes. Sci. 5(1) (2017) 1-11.
[18] D. Baek, S. Saito, K. Takahashi, Estimating work of adhesion using spherical contact between a glass lens and a PDMS block, J. Adhes. Sci. Technol. 32(2) (2018) 158-172.
[19] G. Violano, L. Afferrante, Adhesion of compliant spheres: an experimental investigation, Proc. Struct. Integr. 24 (2019) 251-258.
[20] J.A. Greenwood, K.L. Johnson, The mechanics of adhesion of viscoelastic solids, Philos. Mag. A 43(3) (1981) 697-711.
[21] G. Han, M. Eriten, C.R. Henak, Rate-dependent adhesion of cartilage and its relation to relaxation mechanisms, J. Mech. Behav. Biomed. Mater. 102 (2020) 103493.
[22] V.M. Muller, On the theory of pull-off of a viscoelastic sphere from a flat surface, J. Adhes. Sci. Technol. 13(9) (1999) 999-1016.
[23] M. Poletti, An eye for detail: Eye movements and attention at the foveal scale, Vision Res. 211 (2023) 108277.

[24] J. Iskander, M. Hossny, S. Nahavandi, A Review on Ocular Biomechanic Models for Assessing Visual Fatigue in Virtual Reality, IEEE Access 6 (2018) 19345-19361.
[25] Q. Wei, S. Sueda, D.K. Pai, Physically-based modeling and simulation of extraocular muscles, Prog. Biophys. Mol. Biol. 103(2-3) (2010) 273-283.
[26] A. Shin, L. Yoo, Z. Chaudhuri, J.L. Demer, Independent Passive Mechanical Behavior of Bovine Extraocular Muscle Compartments, Invest. Ophthalmol. Vis. Sci. 53(13) (2012) 8414-8423.
[27] G. Violano, A. Chateauminois, L. Afferrante, Rate-dependent adhesion of viscoelastic contacts, Part I: Contact area and contact line velocity within model randomly rough surfaces, Mech. Mater. 160 (2021) 103926.
[28] G. Violano, A. Chateauminois, L. Afferrante, A JKR-Like Solution for Viscoelastic Adhesive Contacts, Front. Mech. Eng. 7 (2021) 664486.
[29] Z.X. He, Y.H. Yang, H.Y. Jiang, Modeling interfacial instability patterns during debonding a rigid spherical indenter from thin elastic films, J. Mech. Phys. Solids 169 (2022) 105089.
[30] L. Jiang, M.J. Wu, Q.P. Yu, Y.X. Shan, Y.Y. Zhang, Investigations on the Adhesive Contact Behaviors between a Viscoelastic Stamp and a Transferred Element in Microtransfer Printing, Coatings, 2021, p. 1201.
[31] L. Afferrante, G. Violano, On the effective surface energy in viscoelastic Hertzian contacts, J. Mech. Phys. Solids 158 (2022) 104669.
[32] G. Violano, L. Afferrante, Size effects in adhesive contacts of viscoelastic media, Eur. J. Mech. A. Solids 96 (2022) 104665.
[33] J.M. Miller, D.A. Robinson, A model of the mechanics of binocular alignment, Comput. Biomed. Res. 17(5) (1984) 436-470.
[34] J.L. Demer, S.Y. Oh, V. Poukens, Evidence for Active Control of Rectus Extraocular Muscle Pulleys, Invest. Ophthalmol. Vis. Sci. 41(6) (2000) 1280-1290.
[35] R. Kono, R.A. Clark, J.L. Demer, Active Pulleys: Magnetic Resonance Imaging of Rectus Muscle Paths in Tertiary Gazes, Invest. Ophthalmol. Vis. Sci. 43(7) (2002) 2179-2188.
[36] J.L. Demer, Current concepts of mechanical and neural factors in ocular motility, Curr. Opin. Neurol. 19(1) (2006) 4-13.
[37] J.M. Miller, Understanding and misunderstanding extraocular muscle pulleys, J. Vis. 7(11) (2007) 10.
[38] Q. Wei, B. Mutawak, J.L. Demer, Biomechanical modeling of actively controlled rectus extraocular muscle pulleys, Scientific Reports 12(1) (2022) 5806.
[39] A.N. Gent, J. Schultz, Effect of Wetting Liquids on the Strength of Adhesion of Viscoelastic Material, J. Adhes. 3(4) (1972) 281-294.
[40] D. Maugis, M. Barquins, Fracture mechanics and the adherence of viscoelastic bodies, J. Phys. D: Appl. Phys. 11 (1978) 1989-2023.
[41] D. Ahn, K.R. Shull, JKR studies of acrylic elastomer adhesion to glassy polymer substrates, Macromolecules 29(12) (1996) 4381-4390.
[42] B. Lorenz, B.A. Krick, N. Mulakaluri, M. Smolyakova, S. Dieluweit, W.G. Sawyer, B.N.J. Persson, Adhesion: role of bulk viscoelasticity and surface roughness, J. Phys.: Condens. Matter 25(22) (2013) 225004.
[43] E. Barthel, S. Roux, Velocity-Dependent Adherence: An Analytical Approach for the JKR and DMT Models, Langmuir 16(21) (2000) 8134-8138.
[44] D. Maugis, Adherence of elastomers: Fracture mechanics aspects, J. Adhes. Sci. Technol. 1(1)

(1987) 105-134.

[45] G. Violano, G. Orlando, G.P. Demelio, L. Afferrante, Adhesion of viscoelastic media: an assessment of a recent JKR-like solution, IOP Conf. Ser.: Mater. Sci. Eng. 1214(1) (2022) 012038.

[46] Y.Y. Lin, C.Y. Hui, Mechanics of contact and adhesion between viscoelastic spheres: An analysis of hysteresis during loading and unloading, J. Polym. Sci., Part B: Polym. Phys. 40(9) (2002) 772-793.

[47] H. Cheng, M. Li, J. Wu, A. Carlson, S. Kim, Y. Huang, Z. Kang, K.C. Hwang, J.A. Rogers, A Viscoelastic Model for the Rate Effect in Transfer Printing, J. Appl. Mech. 80(4) (2013) 041019.

[48] M.A. Tapia-Romero, M. Dehonor-Gómez, L.E. Lugo-Uribe, Prony series calculation for viscoelastic behavior modeling of structural adhesives from DMA data, Ing., Invest. Tecnol. 21(2) (2020) e1668-e1668.

[49] J. Vroon, J.H. de Jong, A. Aboulatta, A. Eliasy, F.C.T. van der Helm, J.C. van Meurs, D. Wong, A. Elsheikh, Numerical study of the effect of head and eye movement on progression of retinal detachment, Biomech. Model. Mechanobiol. 17(4) (2018) 975-983.

[50] A. Karimi, R. Razaghi, H. Biglari, T. Sera, S. Kudo, Collision of the glass shards with the eye: A computational fluid-structure interaction model, J. Chem. Neuroanat. 90 (2018) 80-86.

[51] X.H. Sun, L.X. Yu, M. Rentschler, H.A. Wu, R. Long, Delamination of a rigid punch from an elastic substrate under normal and shear forces, J. Mech. Phys. Solids 122 (2019) 141-160.

[52] B. Peng, X.Q. Feng, Q.Y. Li, Decohesion of a rigid flat punch from an elastic layer of finite thickness, J. Mech. Phys. Solids 139 (2020) 103937.

[53] I.N. Sneddon, The relation between load and penetration in the axisymmetric boussinesq problem for a punch of arbitrary profile, Int. J. Eng. Sci. 3(1) (1965) 47-57.

[54] M.D. Kern, Adhesion Characterization of a Biologically Inspired Micro-Patterned Synthetic Material, University of Colorado at Boulder, 2016.

[55] H.M. Guo, Z.P. Gao, B.Y. Han, L.J. Zhang, Z.Q. Tang, J. Chen, L.L. Wang, W.Y. Chen, In vivo experimental study on the resistance and stiffness of orbital suspension tissues with/without the extraocular muscles, Biomed. Eng. Online 18(1) (2019) 1-11.

[56] Z.P. Gao, H.M. Guo, W.Y. Chen, Initial tension of the human extraocular muscles in the primary eye position, J. Theor. Biol. 353 (2014) 78-83.

[57] R.A. Clark, J.M. Miller, J.L. Demer, Three-dimensional Location of Human Rectus Pulleys by Path Inflections in Secondary Gaze Positions, Invest. Ophthalmol. Vis. Sci. 41(12) (2000) 3787-3797.

[58] H.M. Guo, Z.P. Gao, W.Y. Chen, Contractile Force of Human Extraocular Muscle: A Theoretical Analysis, Appl. Bionics Biomech. 2016 (2016) 4091824.

[59] C.C. Collins, M.R. Carlson, A.B. Scott, A. Jampolsky, Extraocular muscle forces in normal human subjects, Invest. Ophthalmol. Vis. Sci. 20(5) (1981) 652-664.

[60] S. Schutte, S.P.W. van den Bedem, F. van Keulen, F.C.T. van der Helm, H.J. Simonsz, A finite-element analysis model of orbital biomechanics, Vision Res. 46(11) (2006) 1724-1731.

[61] C. Quaia, H.S. Ying, A.M. Nichols, L.M. Optican, The Viscoelastic Properties of Passive Eye Muscle in Primates. I: Static Forces and Step Responses, PloS one 4(4) (2009) e4850.

[62] J.J. Yang, Q.M. Ren, D. Zhao, Z.P. Gao, X.N. Li, R. He, W.Y. Chen, Corneal Adhesion Possesses the Characteristics of Solid and Membrane, 9(8) (2022) 394.

[63] O. Seijas, P. Gómez de Liaño, P. Merino, C.J. Roberts, R. Gómez de Liaño, Topical anesthesia in strabismus surgery: a review of 101 cases, J. Pediatr. Ophthalmol. Strabismus 46(4) (2009) 218-

222.

[64] M. Naraghi, P.V. Kolluru, I. Chasiotis, Time and strain rate dependent mechanical behavior of individual polymeric nanofibers, J. Mech. Phys. Solids 62 (2014) 257-275.

[65] D. Das, I. Chasiotis, Rate dependent adhesion of nanoscale polymer contacts, J. Mech. Phys. Solids 156 (2021) 104597.

[66] B.C. Jeong, C. Lee, J. Park, D. Ryu, Identification of optimal surgical plan for treatment of extraocular muscle damage in thyroid eye disease patients based on computational biomechanics, Front Bioeng Biotechnol, 2022, p. 969636.

[67] Y.C. Fung, Biomechanics: Mechanical Properties of Living Tissues, Second Edition, New York: Springer1993.

[68] B.A. Nguyen, M.A. Reilly, C.J. Roberts, Biomechanical contribution of the sclera to dynamic corneal response in air-puff induced deformation in human donor eyes, Exp. Eye Res. 191 (2020) 107904.

[69] J. Park, A. Shin, S. Jafari, J.L. Demer, Material properties and effect of preconditioning of human sclera, optic nerve, and optic nerve sheath, Biomech. Model. Mechanobiol. 20(4) (2021) 1353-1363.

[70] H. Hatami-Marbini, M. Pachenari, Tensile Viscoelastic Properties of the Sclera after Glycosaminoglycan Depletion, Curr. Eye Res. 46(9) (2021) 1299-1308.

[71] A.M. Mortazavi, B.R. Simon, W.D. Stamer, J.P. Vande Geest, Drained secant modulus for human and porcine peripapillary sclera using unconfined compression testing, Exp. Eye Res. 89(6) (2009) 892-897.

[72] K.S. Worthington, L.A. Wiley, A.M. Bartlett, E.M. Stone, R.F. Mullins, A.K. Salem, C.A. Guymon, B.A. Tucker, Mechanical properties of murine and porcine ocular tissues in compression, Exp. Eye Res. 121 (2014) 194-199.

[73] D.M. Brown, M.T. Pardue, C.R. Ethier, A biphasic approach for characterizing tensile, compressive and hydraulic properties of the sclera, J. R. Soc. Interface 18(174) (2021) 20200634.

[74] K.R. Shull, Contact mechanics and the adhesion of soft solids, Mater. Sci. Eng. R Rep. 36(1) (2002) 1-45.